

Distribution and fluxes of marine particles in the South China Sea continental slope: implications for carbon export

Shujin Guo^{1,2†}, Mingliang Zhu^{1,2†}, Wenlong Xu³, Shan Zheng^{1,2}, Sumei Liu⁴, Ying Wu⁵, Juan Du^{1,2}, Chenhao Zhao¹, Xiaoxia Sun^{1,2,6}

5 ¹Jiaozhou Bay National Marine Ecosystem Research Station, Institute of Oceanology, Chinese Academy of Sciences, Qingdao 266071, China

²Laboratory for Marine Ecology and Environmental Science, Qingdao Marine Science and Technology Center, Qingdao 266237, China

³Ocean College, Jiangsu University of Science and Technology, Zhenjiang 212100, China

10 ⁴Frontiers Science Center for Deep Ocean Multispheres and Earth System, and Key Laboratory of Marine Chemistry Theory and Technology, Ministry of Education, Ocean University of China, Qingdao 266100, China

⁵State Key Laboratory of Estuarine and Coastal Research, Faculty of Earth Sciences, East China Normal University, Shanghai 201100, China

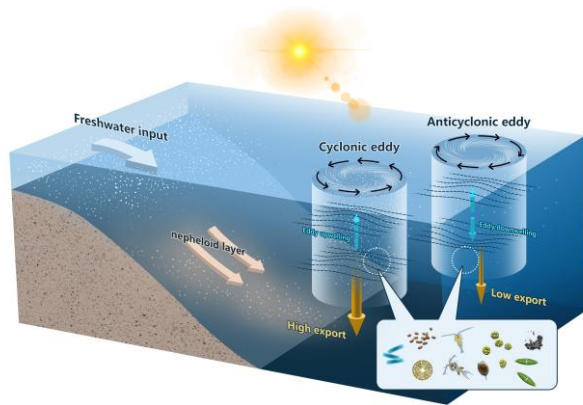
⁶University of Chinese Academy of Sciences, Beijing 100049, China

15 *Correspondence to:* Xiaoxia Sun (xsun@qdio.ac.cn)

Abstract. Marine particles are key vectors in the ocean's biological carbon pump, yet their distribution, size structure, contributions to particulate organic carbon (POC) flux, and the mechanisms controlling these processes remain poorly understood in marginal seas. In this study, we investigated the spatial distribution and carbon flux of marine particles along the continental slope of the South China Sea (SCS), using *in situ* imaging data collected by an Underwater Vision Profiler (UVP 5) during a June 2015 cruise. We also examined how these particle-related processes respond to mesoscale eddy activity. Particle abundance and volume concentration (PVC) ranged from 0 to 783 particles L⁻¹ (mean ± SD: 68 ± 69 particles L⁻¹) and from 0 to 6.7 mm³ L⁻¹ (mean ± SD: 0.3 ± 0.4 mm³ L⁻¹), respectively. Small particles—defined as those with an equivalent spherical diameter (ESD) less than 500 μm—overwhelmingly dominated in terms of abundance, accounting for more than 97% of total counts. However, in terms of PVC, large particles contributed a greater share, averaging 61% ± 12%. PVC was significantly higher in the epipelagic layer (mean ± SD: 0.4 ± 0.7 mm³ L⁻¹) than in the mesopelagic layer (mean ± SD: 0.2 ± 0.1 mm³ L⁻¹, *p* < 0.01), indicating enhanced particle production in surface waters. Under the influence of mesoscale eddies, distinct differences in particle characteristics and carbon export were observed. Cyclonic eddies enhanced particle concentrations and favored the formation of large particles, while anticyclonic eddies were associated with a higher proportion of small particles. These patterns were linked to eddy-induced changes in nutrient availability and phytoplankton production. Consequently, POC fluxes in cyclonic eddy-influenced regions were consistently higher than those in anticyclonic regions throughout the water column, reaching more than twice the values at certain depths. This suggests that mesoscale eddies can influence carbon export by altering both the concentration and size composition of marine particles. Our study clarifies the distribution and size structure of marine particles along the SCS slope and highlights the importance of mesoscale physical processes in regulating particle-mediated carbon export, offering useful references for improving carbon export parameterizations in biogeochemical models.

[†] These authors contributed equally to this work.

Key words: marine particles, Underwater Vision Profiler, [particle distribution, size structure, mesoscale eddies,](#) particulate organic carbon (POC) flux, [particle size distribution, mesoscale eddies,](#) South China Sea, continental slope, [biological pump](#)



1 Introduction

Marine particles are critical components of the oceanic carbon cycle, serving as vehicles for transporting organic carbon from the surface ocean to the deep sea via the biological pump (Siegel et al., 2022). These particles, which include a diverse array of forms such as micron-scale phytoplankton cells, submillimeter detrital fragments, millimeter-scale aggregates, and zooplankton fecal pellet, play an essential role in global carbon dynamics (Turner, 2015). [The abundance and distribution of marine particles are regulated by a combination of abiotic and biotic factors, such as primary productivity, particle aggregation and fragmentation, as well as hydrodynamic conditions all interact to shape particle fields in the ocean \(Forest et al., 2012; Kiko et al., 2022\).](#) The transport of marine particles from surface waters to deeper layers is a primary mechanism for sequestering carbon in the deep ocean, effectively isolating it from the atmosphere for timescales ranging from decades to millennia, leading to a decrease in atmospheric CO₂ (Kwon et al., 2009; Boyd et al., 2019). Due to the widespread vertical settling behavior of particles in the ocean, their abundance and size not only influence the efficiency of the carbon export but also govern the biogeochemical pathways through which carbon is transformed, remineralized, or permanently stored in the ocean's interior (Kiko et al., 2022). Therefore, [understanding the distribution, size structure, and associated carbon export of marine particles is critical for assessing the efficiency of the biological carbon pump, the study on distribution characteristics of marine particles, their size composition, and their associated carbon export flux is crucial for gaining a comprehensive understanding of biogeochemical cycles, particularly the carbon cycle in the ocean.](#)

Although marine particles play a crucial role in ocean biogeochemical cycles, their fragile nature poses significant challenges for collection and analysis. Sediment traps have been widely employed to capture settling particles and quantify vertical fluxes ([Honjo et al., 2008; Harms et al., 2021; Ramondenc et al., 2016](#)). While this method provides valuable insights, it lacks the spatial coverage and detailed particle size distribution data necessary for a mechanistic understanding of particle dynamics (Wang et al., 2024a). In recent years, advancements in *in situ* optical and imaging technologies have introduced an alternative approach for assessing particle distribution and estimating fluxes (Picheral et al., 2010; Boss et al., 2015). The Underwater Vision

70 Profiler (UVP) has emerged as a powerful tool, enabling high-resolution, *in situ* measurements of particle size distribution and abundance across a broad depth range (Picheral et al., 2010). The compact design of the UVP allows for integration with conductivity, temperature, and depth (CTD) rosette samplers as well as deployment on small autonomous platforms such as underwater gliders (Picheral et al., 2022). When combined with image processing techniques for particle identification, the UVP facilitates comprehensive characterization of particle abundance, size, composition, and potential sources (Trudnowska et al., 2021, 2023), thereby enhancing our understanding of particle formation and transformation processes. Beyond particle characterization, the UVP has been instrumental in estimating particle fluxes by leveraging empirical relationships between particle size and sinking flux (Guidi et al., 2008a; Iversen et al., 2010; Guidi et al., 2016; Ramondenc et al., 2016; Wang et al., 2024b). These flux estimations are derived from *in situ* observations of particle size distributions, where particle abundance is expressed as a function of size (Guidi et al., 2008a; Fender et al., 2019). The high vertical resolution of UVP observations in marine particles, coupled with established size-dependent relationships for carbon content and sinking velocity (Kriest, 2002; Guidi et al., 2008a; Clements et al., 2023), provides a uniquely detailed perspective on the three-dimensional distribution of particulate organic carbon (POC) flux in the ocean (Guidi et al., 2016; Kiko et al., 2017; Cram et al., 2018). Observations from the UVP5 have been employed to quantify regional POC fluxes from the surface ocean (Forest et al., 2012; Kiko et al., 2017; Cram et al., 2018) and to reconstruct large-scale carbon export patterns across diverse oceanic biomes (Guidi et al., 2015; Wang et al., 2024b). These advancements underscore the critical role of UVP-based observations in refining our understanding of oceanic carbon cycling and particle-mediated export processes.

Mesoscale eddies, as ubiquitous and energetic features in the global ocean, have been extensively studied for their roles in regulating physical dynamics, biogeochemical processes, and ecosystem structures (McGillicuddy Jr et al., 2016). Numerous studies have demonstrated that eddies can significantly influence nutrient transport, primary productivity, and biological community composition in the ocean (Stramma et al., 2013; Zhang et al., 2020; Barone et al., 2022). Cyclonic eddies generally induce upwelling that brings cold, nutrient-rich subsurface water into the euphotic zone, thereby stimulating new production and enhancing phytoplankton biomass (Shih et al., 2020). This nutrient enrichment often favors the growth of large-sized phytoplankton, particularly diatoms, leading to a community shift toward a more productive, herbivore-based food web (Barlow et al., 2014; Wang et al., 2016). In contrast, anticyclonic eddies are typically characterized by downwelling and enhanced water column stratification, which suppress vertical nutrient supply, leading to reduced surface productivity and a food web dominated by smaller phytoplankton and microbial pathways (Peterson et al., 2005; Stramma et al., 2013). Despite these advances, our understanding of how mesoscale eddies influence the distribution and size structure of marine particles remains limited, particularly in marginal seas. Key questions remain unanswered: To what extent do mesoscale eddies regulate particle abundance and size composition? Do cyclonic and anticyclonic eddies exert distinct influence due to their contrasting physical and biogeochemical characteristics? And critically, how do these differences in particle dynamics translate into variability in vertical carbon export? The lack of observations and systematic analyses on particle size structure and vertical fluxes under the influence of mesoscale eddies hampers accurate assessments of biological pump efficiency in the ocean. Therefore, elucidating the impacts of mesoscale eddies on particles characteristics, including abundance, size composition, and vertical transport potential, is essential for improving our understanding of oceanic carbon cycling and enhancing the reliability of biogeochemical models.

The South China Sea (SCS) is one of the largest semi-enclosed marginal seas, characterized by a narrow

带格式的: 字体颜色: 文字 1

110 and steep continental slope in its northern region (Zhang et al., 2020). The northern SCS is influenced by a
complex interplay of oceanographic and atmospheric processes, including the monsoon system, frequent
115 typhoons, seasonal intrusions of the Kuroshio Current, and freshwater inputs from the Pearl River (Dai et al.,
2020). In addition, mesoscale eddies are frequently observed in the SCS, with Kuroshio Current intrusions
playing a dominant role in their formation, particularly in the northern region (Xiu et al., 2010). The continental
slope of the SCS serves as a transitional zone between the nutrient and chlorophyll *a* (Chl *a*) rich shelf waters
and the oligotrophic open ocean, playing a crucial role in regulating material and energy exchange between these
120 two systems (Zhang et al., 2023). This slope features a rapid bathymetric gradient, with depths increasing
sharply from less than 200 m at the shelf break to over 1000 m. The region is influenced by multiple water
masses, including Kuroshio intrusions, a southwestward along-slope current, and cross-slope transport of fresher
water originating from the Pearl River (Wang et al., 2019). These unique hydrographic conditions exert complex
influence on the production, aggregation, and sinking of marine particles (Turner et al., 2017), making the region
125 a critical yet underexplored area for understanding particle-mediated carbon export. Mesoscale eddies are
ubiquitous in the slope region of the SCS, where both cyclonic and anticyclonic eddies frequently occur due to
the combined influence of monsoonal winds, Kuroshio intrusion, and complex topography (Wu and Chiang,
2007; Shih et al., 2020; Zhang et al., 2020). Typically spanning 100–200 km in diameter and persisting for
weeks to months, these eddies exhibit pronounced seasonal variability (Wu and Chiang, 2007). Cyclonic eddies
130 are more prevalent during the summer months, driven by enhanced upwelling and the southwesterly monsoon,
whereas anticyclonic eddies are more frequently observed in winter and early spring, often formed as warm-core
rings shed from the Kuroshio Current loop (Shih et al., 2020; Zhang et al., 2020). These eddies propagate
predominantly westward or southwestward along the northern continental slope of the SCS, significantly
modulating the vertical structure of temperature, salinity, and nutrient fields in this region (Guo et al., 2015).
135 While the impacts of mesoscale eddies on physical circulation, nutrient dynamics, and phytoplankton community
structures have been relatively well studied in this region (Wu and Chiang, 2007; Xiu and Chai, 2011; Wang et
al., 2016; Xu et al., 2025), their influence on the distribution and size structure of marine particles, especially in
the context of carbon export processes, remains insufficiently explored. The information on particle size
distribution, which is essential for understanding the mechanisms of particle transformation, sinking behavior,
and carbon sequestration efficiency, is also quite limited. This lack of direct observational constraints hampers
our ability to evaluate the role of marine particles size in modulating carbon export pathways and their sensitivity
to mesoscale variability.

Several studies have investigated particle export fluxes in the SCS. Li et al. (2017) analyzed POC sinking
140 fluxes at a depth of 1200 m in the central SCS using a seven-year time series of sediment trap observations,
revealing that the East Asian Monsoon and mesoscale eddies jointly regulate POC flux variability. Zhou et al.
(2020) examined the temporal variations in ²³⁴Th-based particle export from 2004 to 2014 at the South East
Asian Time-series Study (SEATS) site and found that particle flux increased with mixed layer depth, particularly
in winter, due to the influence of the strong northeast monsoon. Hong et al. (2021) quantified cross-shelf POC
145 export in the northern SCS shelf using ²³⁴Th-based estimates and sediment traps, reporting a vertical POC flux of
26 mmol m⁻² d⁻¹ from the euphotic zone and a cross-shelf transport flux of 9.9 mmol m⁻² d⁻¹. Ma et al. (2023)
investigated nutrient-dependent export productivity structures within the euphotic zone of the oligotrophic SCS
basin, highlighting that even the nutrient-depleted layer can act as a net exporter of POC. Despite these valuable

带格式的: 字体: Times New Roman

150 contributions, most previous studies have relied on sediment traps or radionuclide-based methods, which provide limited information on the size structure and vertical evolution of particle fluxes. In particular, *in situ*, size-resolved observations that link particle abundance, size composition, and export efficiency under dynamic physical forcing (e.g., eddies) remain scarce in the SCS slope region. This lack of direct observational constraints hampers our ability to evaluate the role of particle size in modulating carbon export pathways and their sensitivity to mesoscale variability.

155 This study aims to address these knowledge gaps by analyzing high-resolution UVP data collected from the continental slope of the SCS during a 2015 survey, during which an anticyclonic-cyclonic eddy pair was observed. Specifically, our objectives are to (1) characterize the spatial distribution patterns of marine particles, both horizontally and vertically, (2) quantify the POC flux associated with particle sedimentation and compare the relative contributions of particles with different sizes, and (3) investigate the influence of mesoscale eddies on particle dynamics and carbon export processes in this region. Unlike previous studies that primarily focused on surface-derived carbon fluxes or bulk particle inventories, this study integrates size-resolved, *in situ* particle observations with empirical flux estimates to examine depth-dependent export processes along a dynamic continental slope. These findings contribute to a better understanding of the spatial heterogeneity and controlling factors of the biological pump in the SCS, and offer process-level observational constraints that can inform carbon flux modeling in other oligotrophic slope systems. This study aims to fill the existing knowledge gaps by
160 analyzing high-resolution UVP data collected along the continental slope of the SCS during a 2015 cruise, during which a mesoscale anticyclonic-cyclonic eddy pair was observed. Specifically, the objectives of this study are to (1) provide the first detailed characterization of the spatial distribution of marine particles along the SCS continental slope and identify the key environmental factors driving their variability, (2) analyze the size composition of particles and evaluate its implications for carbon cycling, and (3) investigate the mechanisms by which mesoscale eddies modulate particles dynamics and their associated POC fluxes in this region. This study
165 will provide new insights into how eddy-induced physical variability regulates particle dynamics and their associated vertical transfer in the SCS, and hold important implications for improving carbon flux parameterizations in marginal seas and other oligotrophic systems.

带格式的：字体：10 磅

带格式的：字体：10 磅

带格式的：字体：10 磅

带格式的：字体：10 磅

带格式的：字体：10 磅

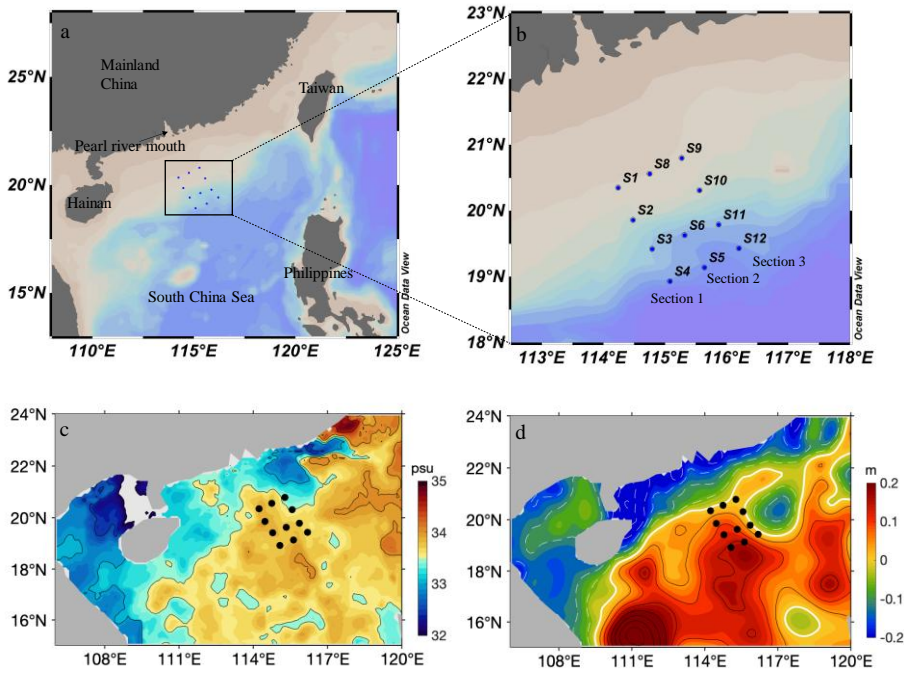
带格式的：字体：10 磅

175 2 Material and methods

2.1 Surveyed area and data acquisition

A research cruise was carried out in the SCS aboard the research vessel *Nanfeng* from June 13 to June 29, 2015. The study area and survey stations were shown in Fig. 1a. The survey stations can be divided into three transects (Transect 1, Transect 2, and Transect 3) (Fig. 1b), which extend across the slope of the SCS, with
180 shallower sites at over 100 m and deeper sites exceeding 1000 m in depth (Table 1). Satellite data were used to analyze the spatial and temporal variations in the physical and dynamic characteristics of the study region. The Sea Surface Salinity (SSS) data consists of daily global, gap-free Level-4 (L4) analyses of SSS at a resolution of 1/8°. These analyses are generated through a multivariate optimal interpolation algorithm that combines SSS data from different satellite sources, including NASA's Soil Moisture Active Passive (SMAP) and ESA'S Soil
185 Moisture Ocean Salinity (SMOS) satellites, along with *in situ* salinity measurements provided by the Copernicus Marine Environment Monitoring Service (Multi Observation Global Ocean Sea Surface Salinity and Sea Surface Density) (Buongiorno Nardelli et al., 2016; Sammartino et al., 2022). Eddies were identified as local minima

(cyclonic eddies) and maxima (anticyclonic eddies) in sea level anomaly (SLA) using a composite altimetry product, which is based on a combination of remote sensing observations distributed by the Copernicus Marine Environment Monitoring Service (SEALEVEL_GLO_PHY_CLIMATE_L4_MY_008_057).



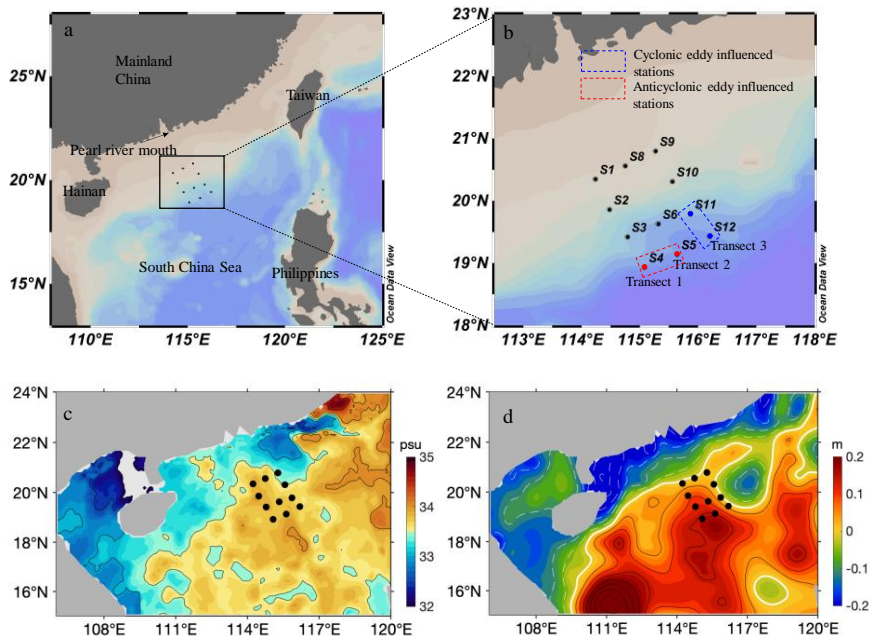


Fig. 1 Study area and survey stations in the SCS continental slope. a: the study region; b: the enlarge view; c: sea surface salinity (SSS) at $1/8^\circ$ of resolution; d: sea level anomalies (SLA). The dots indicate the locations of the sampling stations. Red dots indicate stations influenced by the anticyclonic eddy, and blue dots represent stations located at the periphery of the cyclonic eddy.

197 Table 1. Location and deployment times of UVP in the study area. UVP deployment depth refers to the
 198 maximum depth reached during each profile. Sampled volume represents the total volume imaged by the
 199 UVP during each deployment. Station 7 was skipped due to instrument malfunction, and therefore not
 200 included in this study.

Station	Longitude (°E)	Latitude (°N)	Date	Time (hh:mm. UTC + S)	Bottom depth (m)	UVP deployment depth (m)	Total particles ($\times 10^4$ #)	Sampled volume ($\times 10^3$ L)
S1	114.40	20.29	18- June- 2015	02:40 p.m.	123	110	<u>101.74</u>	<u>5.99</u>
S2	114.47	19.87	17- June- 2015	03:45 a.m.	587	500	<u>182.55</u>	<u>12.80</u>
S3	114.79	19.42	16- June- 2015	01:35 p.m.	1300	800	<u>52.73</u>	<u>13.85</u>
S4	115.08	18.93	15- June- 2015	11:45 p.m.	3000	800	<u>64.79</u>	<u>15.39</u>
S5	115.64	19.14	15- June- 2015	07:30 a.m.	2800	800	<u>65.49</u>	<u>15.04</u>
S6	115.32	19.63	14- June- 2015	03:25 p.m.	2108	800	<u>66.24</u>	<u>15.77</u>
S8	114.75	20.56	18- June- 2015	08:50 p.m.	120	100	<u>95.83</u>	<u>6.47</u>
S9	115.27	20.80	19- June- 2015	08:15 a.m.	170	110	<u>49.97</u>	<u>7.28</u>
S10	115.56	20.31	19- June- 2015	07:30 p.m.	560	500	<u>69.98</u>	<u>5.84</u>
S11	115.86	19.78	20- June- 2015	01:20 p.m.	1556	800	<u>131.91</u>	<u>15.25</u>
S12	116.20	19.43	21- June- 2015	01:45 p.m.	1971	800	<u>51.39</u>	<u>5.64</u>

- 带格式表格
- 带格式的：字体：Times New Roman
- 带格式的：字体：Times New Roman
- 带格式的：字体：Times New Roman
- 带格式的：上标

201

202 Hydrographic measurements and water sampling were conducted using an SBE911 plus dual
203 conductivity-temperature-depth (CTD) sensor unit coupled with an SBE 32 Water Sampler (Seabird
204 Scientific, Bellevue, WA, USA). The CTD system recorded profiles of temperature ($^{\circ}\text{C}$), salinity (psu),
205 and pressure (dbar) profiles throughout the water column.

206 Nutrients and chlorophyll *a* (Chl *a*) concentrations were determined from seawater samples
207 collected at multiple depths using a 10 L Niskin sampler (KC-Denmark Inc., Denmark) deployed
208 alongside a CTD. For nutrient analysis, seawater samples were filtered through a 0.45 μm pore-size
209 cellulose acetate membrane, and the filtrates were stored at temperatures below -20°C until further
210 processing. In the laboratory, nutrient concentrations were measured using a Technicon AA3
211 autoanalyzer (Bran-Luebbe GmbH) following standard protocols (Liu et al., 2022). The detection limits
212 for nutrient analysis were $0.02\ \mu\text{mol L}^{-1}$ for NO_3^- , $0.01\ \mu\text{mol L}^{-1}$ for NO_2^- , $0.03\ \mu\text{mol L}^{-1}$ for PO_4^{3-} , and
213 $0.05\ \mu\text{mol L}^{-1}$ for SiO_3^{2-} . Chl *a* concentrations were determined using the fluorometric method
214 (Welschmeyer, 1994). Seawater samples (500 mL) were filtered through 0.7 μm Whatman GF/F filters,
215 and pigments were extracted in 90% acetone at 4°C in the dark for 24 h. Fluorescence measurements
216 were then conducted using a Turner Designs fluorometer (Model 10).

217 2.2 Particle measurement

218 Particle size and abundance were measured using a high-resolution, high-frequency Underwater
219 Vision Profiler (UVP 5.0-HD). The UVP was mounted downward-facing on the CTD Niskin-rossette,
220 and vertical deployments were conducted at a descent speed of 1 m/s. The UVP captured images of
221 illuminated particles within a known sampling volume of $1.053\pm 0.53\ \text{L per frame}$. Particle size was
222 determined based on the number of pixels in the captured images. Size and volume calibrations were
223 performed in a seawater tank using natural particles of various types to establish the pixel-to-metric
224 unit conversion (Picheral et al., 2010). Images were recorded digitally at a rate of 12 frames per second
225 and processed using custom developed image analysis software. The equivalent spherical diameter
226 (ESD) of each particle was calculated under the assumption that the particle's projected shape was
227 circular. Particle volume concentration (PVC) was calculated by summing the estimated volumes of all
228 particles detected within each depth bin and normalizing by the corresponding sampled water volume.
229 The volume of each particle was estimated by assuming spherical geometry based on the ESD. The

带格式的: 字体: Times New Roman

230 final PVC is reported in $\text{mm}^3 \text{L}^{-1}$.

231 Previous inter-calibration studies of UVP systems have shown that only the overlapping size
232 ranges among different studies are suitable for comparative particle profile analyses (Guidi et al.,
233 2008a; Picheral et al., 2010). For consistency with previous studies, we set the upper size limit for
234 particle flux calculations at 1.5 mm ESD (Guidi et al., 2007, 2008a; Stemmann et al., 2008;
235 Ramondenc et al., 2016). The lower size limit was set at 100 μm ESD to exclude signals potentially
236 caused by camera resolution constraints and background noise, which could not be reliably
237 distinguished as actual particles (Fender et al. 2019). For data visualization in this study, particles
238 ~~abundance was/were~~ categorized following Kiko et al. (2022) into two groups: small particles ($\text{ESD} <$
239 0.50 mm) and large particles ($\text{ESD} \geq 0.50 \text{ mm}$). ~~This classification provides insights into size-~~
240 ~~dependent particle dynamics, including aggregation, disaggregation, and vertical transport~~
241 ~~processes. This classification enables the examination of size-dependent vertical distribution patterns,~~
242 ~~which can reflect underlying processes such as aggregation near the surface, disaggregation at depth,~~
243 ~~and differential sinking behavior of particles of varying sizes.~~

244 To assess the influence of mesoscale eddies on the biological component of the particle field,
245 large particles were classified into living and non-living categories. In this context, living particles refer
246 specifically to large zooplankton, while all others were categorized as non-living particles. We
247 extracted and analyzed zooplankton data from the UVP imagery. Due to the resolution limitations of
248 the UVP5, small particles could not be reliably imaged or morphologically classified in this study.
249 Vignette images of large particles were extracted from the UVP5-HD dataset and used for zooplankton
250 classification. The extracted images were uploaded to the EcoTaxa platform (<https://ecotaxa.obs->
251 [vlfr.fr](https://ecotaxa.obs-vlfr.fr)), where a machine learning classifier (random forest algorithm) was applied to assign objects
252 into broad morphological categories, including zooplankton and non-living particles (Picheral et al.,
253 2017). All classified images were then visually checked and corrected by trained analysts to ensure
254 taxonomic accuracy. The abundance of zooplankton (ind. L^{-1}) was calculated by dividing the number of
255 individuals identified in each depth bin by the corresponding volume of water imaged by the UVP.

256 2.3 Estimation of POC export flux from particle size spectrum

257 The POC export flux was estimated from particle size spectra using the method developed by
258 Guidi et al. (2008a, b). The particle size distribution (PSD) generally follows a power-law decrease

域代码已更改

259 over the μm to mm size range (Guidi et al., 2009). This distribution, derived from UVP images, is
 260 expressed as:

261
$$n(d) = \alpha d^\beta \quad (1)$$

262 where d (mm) represents particles diameter, $n(d)$ is the particle size spectrum, α is normalization
 263 constant and β is the exponent characterizing the slope of the number spectrum after log
 264 transformation. The particle size-based carbon flux approach assumes that the total carbon flux, (F)
 265 ($\text{mg C m}^{-2} \text{d}^{-1}$), corresponds to the integration of the flux spectrum over all particle sizes, from the
 266 smallest (d_{\min}) to the largest (d_{\max}) diameterparticle size:

267
$$F = \int_{d_{\min}}^{d_{\max}} n(d) \cdot m(d) \cdot w(d) dd \quad (2)$$

268 where $n(d)$ is the particle number spectrum (particles $\text{m}^{-3} \text{mm}^{-1}$), $m(d)$ (mg C) is represents the carbon
 269 mass (carbon content) of a particle with diameter d spherical partiele, and $w(d)$ (m d^{-1}) is its sinking
 270 velocity, estimated using Stokes' Law.

271 The combined particle mass and settling velocity follow a power-law function of particle
 272 diameter, based on empirical relationships derived from comparisons of PSDs obtained through
 273 imaging systems and sediment trap mass flux estimates (Guidi et al., 2008a; Jouandet et al., 2011). This
 274 relationship is expressed as: $m(d) \cdot w(d) = Ad^B$, where A (mg C m d^{-1}) and B are empirical constants. The
 275 particle carbon flux can thus be approximated by discretizing Equation (2) into small logarithmic
 276 diameter intervals (Guidi et al., 2009; Picheral et al., 2010):

277
$$F = \sum_{i=1}^x n_i A d_i^B \Delta d_i \quad (3)$$

278 where $A = 12.5 \pm 3.40$ and $B = 3.81 \pm 0.70$, representing the best-fit parameters that minimized log-
 279 transformed discrepancies between global oceanic sediment trap-derived carbon flux estimates and
 280 UVP-derived particle abundance and PSDs (Guidi et al., 2008a). This approach has been widely
 281 applied in various oceanic regions worldwide in recent years (Iversen et al., 2010; Ramondenc et al.,
 282 2016; Fender et al., 2019; Clements et al., 2023; Wang et al., 2024a, b).

283 **2.4 Data analysis**

284 All particle size and abundance data obtained from the UVP were binned into 5 m vertical intervals
 285 and subsequently processed to generate depth profiles of particle abundance, particle volume
 286 concentration ($\text{mm}^3 \text{L}^{-1}$), and POC flux ($\text{mg C m}^{-2} \text{d}^{-1}$). To visualize along-slope variability, section plots

287 were created for each transect by interpolating the depth-resolved particle abundance, volume
288 concentration, and POC flux across stations. Statistical analyses were performed using SPSS 25.0. Two-
289 tailed independent-sample *t*-tests were conducted to assess significant differences in particle and flux
290 parameters between different depth layers and regions. Prior to applying *t*-tests, data normality and
291 variance homogeneity were tested using the Shapiro-Wilk and Levene's tests, respectively (González-
292 Estrada and Cosmes, 2019). For data not meeting parametric assumptions, non-parametric alternatives
293 were used. Pearson correlation analysis (PCA) was applied to evaluate the relationships between POC
294 flux and environmental variables. Significance was defined at $p < 0.05$ unless otherwise stated.
295 Hydrographic and particle data were visualized using Ocean Data View 4 and Origin 2022.

296

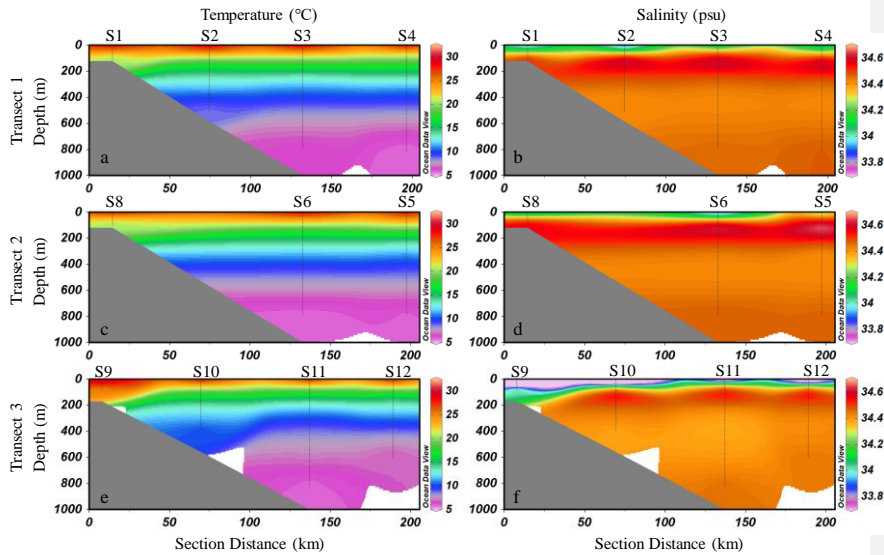
297 3 Results

298 3.1 Hydrographic conditions

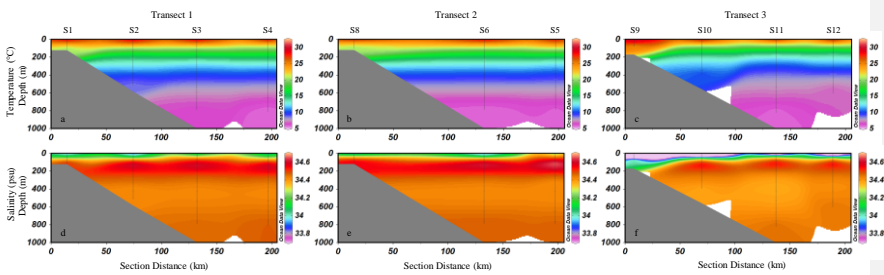
299 Based on the spatial distribution of SLA, two mesoscale eddies were present in the study area
300 during the survey period: one cyclonic eddy and one anticyclonic eddy (Fig. 1d). Stations S4 and S5,
301 located on the outer edge of Transects 1 and 2, respectively, were situated in a region where SLA
302 exceeded +0.1 m, indicating influence from an anticyclonic eddy. In contrast, a distinct cyclonic eddy
303 with SLA values below -0.1 m was present to the east of stations S11 and S12 in Transect 3. These
304 two stations were positioned along the periphery of the cyclonic eddy, where the SLA gradient was
305 steep. The outer stations of Transects 1 and 2, S4 and S5, were influenced by the anticyclonic eddy,
306 whereas stations S11 and S12 in Transect 3 were located at the periphery of the cyclonic eddy. Based
307 on the distribution of sea surface salinity (SSS) (Fig. 1e), the salinity at stations S9 and S10 along
308 Transect 3 was lower than at other stations. In situ CTD measurements further confirmed that the upper
309 water column at these stations exhibited reduced salinity (Supplementary Fig. S1f), indicating a certain
310 degree of influence from the Pearl River plume. Vertically, the study area exhibits distinct
311 characteristics of a tropical ocean, with relatively high sea surface temperature (~30 °C) and strong
312 stratification in the upper 200 m (Fig. 2). A pronounced thermocline is observed between 100 and 200
313 m, marking a sharp temperature gradient (Fig. 2a, c and e). Salinity increases with depth, further
314 reinforcing the stratification pattern (Fig. 2b, d and f).

带格式的: 字体: Times New Roman

带格式的: 字体: Times New Roman



315



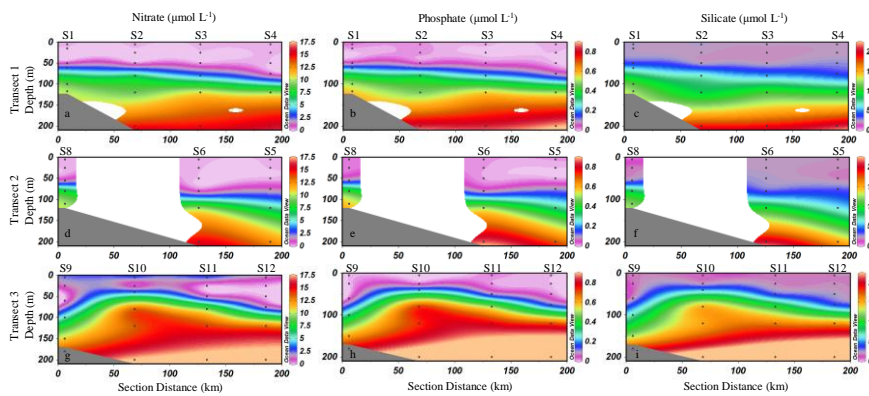
316

317 **Fig. 2. Vertical distribution of temperature (a-c, °C) and salinity (d-f, psu) along the three transects in the**
 318 **study area. Transect 1: temperature (a, °C), salinity (b, psu); Transect 2: temperature (c, °C), salinity (d,**
 319 **psu); Transect 3: temperature (e, °C), salinity (f, psu)**

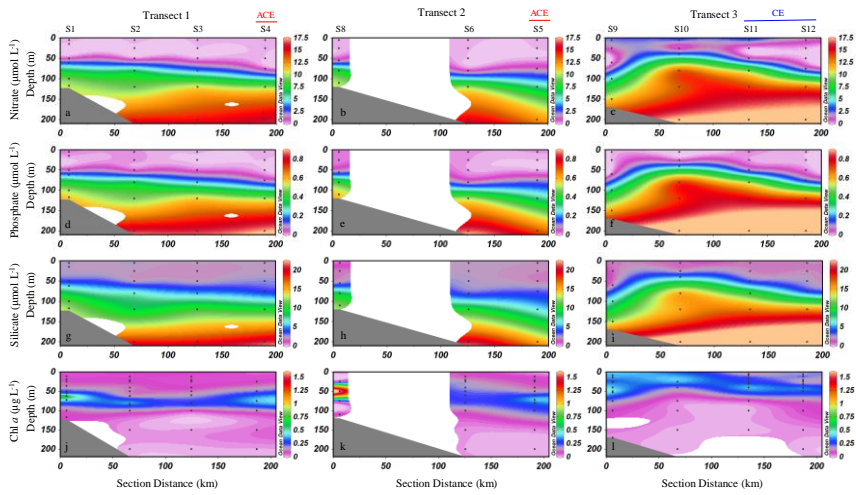
320 The sectional distributions of nutrients in the study area are presented in Fig. 3. The nutrient
 321 distribution follows the typical characteristics of tropical oligotrophic waters, with low nutrient
 322 concentrations in the upper water column and a pronounced nutricline occurring between 50 and 100 m,
 323 where nutrient concentrations increase sharply (Fig. 3). At most stations, surface nitrate concentrations
 324 were below the detection limit, except for Transect 3. At the inner station of Transect 3 (S9), the surface
 325 nitrate concentration was $2.3 \mu\text{mol L}^{-1}$. The outer stations of Transect 3, S11 and S12, exhibited surface
 326 nitrate concentrations of $2.8 \mu\text{mol L}^{-1}$ and $1.33 \mu\text{mol L}^{-1}$, respectively. These values were significantly
 327 higher than those observed at surface waters of Transects 1 and 2 (*t* test, $p < 0.01$), where nitrate

328 concentrations generally remained below $0.1 \mu\text{mol L}^{-1}$ (Fig. 3a, d). Phosphate and silicate exhibit
 329 distribution patterns similar to those of nitrate. The concentrations of nitrate and phosphate in the upper
 330 50 m were generally higher at the cyclonic eddy stations (S11, S12) compared to the anticyclonic eddy
 331 stations (S4, S5) (*t*-test, $p < 0.01$), and silicate concentrations were relatively consistent across these
 332 stations (Supplementary Fig. S2). The sectional distributions of nutrients and Chl *a* concentrations in the
 333 study area are shown in Fig. 3. Nutrient profiles exhibit typical oligotrophic features, with low
 334 concentrations in surface waters and a pronounced nutricline between 50 and 100 m. Chl *a* exhibited a
 335 pronounced Deep Chlorophyll Maximum (DCM), especially along Transect 1 and 2 (Fig. 3j, k). Along
 336 Transect 3, the depth of the DCM became shallower, and Chl *a* concentrations were relatively high
 337 throughout the upper layer at nearshore stations (Fig. 3i). Vertically, there were clear differences in the
 338 distribution of nutrients and Chl *a* between stations influenced by the anticyclonic eddy (S4, S5) and
 339 those influenced by the cyclonic eddy (S11, S12) (Supplementary Fig. S1). Nutrient concentrations at
 340 stations S11 and S12 were generally higher than those at stations S4 and S5 from 0 to 200 m
 341 (Supplementary Fig. S1a-c). Chl *a* concentrations at depths shallower than 50 m were higher at stations
 342 S11 and S12 than at the same depths at stations S4 and S5 (Supplementary Fig. S1d). With increasing
 343 depth, Chl *a* levels at S11 and S12 gradually declined, whereas those at S4 and S5 continued to rise,
 344 peaking at approximately 75 m before decreasing again.

345



346



347

348 **Fig. 3. Sectional distribution of nutrient concentrations (nitrate, phosphate, and silicate) ($\mu\text{mol L}^{-1}$) and Chl**
 349 ***a* concentrations ($\mu\text{g L}^{-1}$) in the upper 200 m of the study area. a-c: nitrate ($\mu\text{mol L}^{-1}$); d-f: phosphate (μmol**
 350 ***L}^{-1}); g-i: silicate ($\mu\text{mol L}^{-1}$); j-l: Chl *a* ($\mu\text{g L}^{-1}$). ACE denotes stations influenced by the anticyclonic eddy,***
 351 **while CE denotes stations influenced by the cyclonic eddy. Transect 1: nitrate (a, $\mu\text{mol L}^{-1}$), phosphate (b,**
 352 **$\mu\text{mol L}^{-1}$), silicate (c, $\mu\text{mol L}^{-1}$); Transect 2: nitrate (d, $\mu\text{mol L}^{-1}$), phosphate (e, $\mu\text{mol L}^{-1}$), silicate (f, $\mu\text{mol L}$**
 353 **$^{-1}$); Transect 3: nitrate (g, $\mu\text{mol L}^{-1}$), phosphate (h, $\mu\text{mol L}^{-1}$), silicate (i, $\mu\text{mol L}^{-1}$)**

The sectional profiles of Chl *a* concentration reveal significant spatial variability in primary productivity across the study area (Fig. 4). In Transect 1, a pronounced subsurface chlorophyll maximum (SCM) is observed at approximately 50–100 m depth, particularly near the coastal stations, where Chl *a* concentrations exceed $0.6 \mu\text{g L}^{-1}$ (Fig. 4a). In Transect 2, the SCM is most prominent at the nearshore station, where the highest Chl *a* concentration of $1.6 \mu\text{g L}^{-1}$ occurs around 50 m depth. As the transect extends offshore, the SCM becomes less pronounced, with peak Chl *a* concentrations ranging from 0.2 to $0.4 \mu\text{g L}^{-1}$. In Transect 3, relatively high Chl *a* concentrations are observed in the upper 50 m at the nearshore station (Fig. 4c). Further offshore, Chl *a* concentrations decrease, forming a well-defined SCM. At the outermost station, relatively elevated Chl *a* concentrations persist in the upper 50 m. The Chl *a* concentrations in the upper 50 m at the cyclonic eddy-influenced stations S11 and S12 were higher than those at the anticyclonic eddy-influenced stations S4 and S5 (Supplementary Fig. S2d).

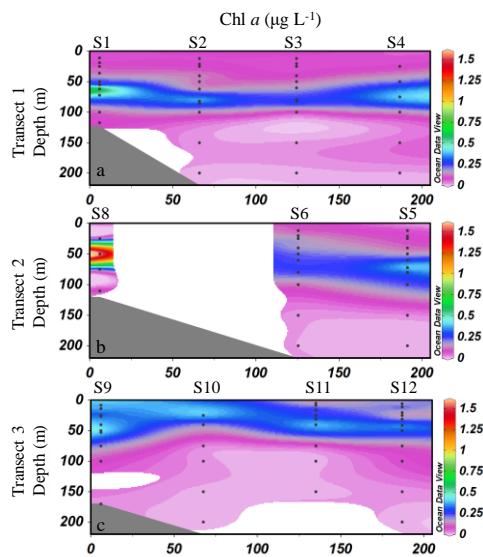


Fig. 4. Sectional distributions of Chl *a* ($\mu\text{g L}^{-1}$) along the three transects in the study area. a: Transect 1; b: Transect 2; c: Transect 3

3.2 Particle concentration and size structure distribution

Particle abundances ranged from 0 to 783 particles L^{-1} , with a mean of 68 ± 68 particles L^{-1} (mean \pm SD).

The vertical profiles of particle abundance across the three transects exhibited distinct spatial and depth-related variations (Fig. 45). In Transect 1, high particle abundance was observed in the bottom waters of the nearshore station S1 and the slope station S2, with values reaching up to 700 particles L^{-1} at 500 m depth at station S2 (Fig. 45a). Notably, the vast majority of particles at this depth were small particles ($\text{ESD} < 500 \mu\text{m}$), accounting for over 99% of the total particle abundance (Fig. 4d5b). Additionally, a slight increase in particle abundance was observed in the 60–80 m layer at the outer slope station S4. In Transect 2, particle abundance gradually decreased from the inner shelf to the outer slope and from surface to bottom waters (Fig. 4b5d). In Transect 3, a distinct peak in particle

带格式的: 字体: Times New Roman

abundance was observed at 379–390 m depth at the slope station S10 (Fig. 4c5g). Furthermore, at the outermost stations S11 and S12, elevated particle concentrations were observed in the upper 50 m of the water column, with peak values reaching up to 200 particles L⁻¹. This is notably significantly higher than the maximum particle abundances recorded at stations station S4 and S5, where values remained below 150 particles L⁻¹ (Fig. 45a, d). The distribution patterns of zooplankton (Supplementary Fig. S2) in the study area were generally similar with that of particle abundances. On transects 1 and 2, higher zooplankton abundances were observed at the nearshore stations, with a decreasing trend toward offshore stations (Supplementary Fig. S2a, b). In contrast, on transect 3, elevated abundances were recorded at the outer stations S11 and S12 (Supplementary Fig. S2c). At 20 m depth at station S11, zooplankton abundance reached as high as 0.7 ind. L⁻¹. The distribution pattern of non-living particles closely mirrored that of zooplankton, with concentrations observed at the nearshore stations of transects 1 and 2, as well as in the upper to mid-depth waters at stations S11 and S12 on transect 3 (Supplementary Fig. S2d-f). Regarding particle size composition, small particles overwhelmingly dominated the total particle abundance, consistently accounting for more than 97% across all transects and throughout the water column (Fig. 4d-f5b-e, h). In contrast, large particles contributed only a minor fraction of the total abundance at all depths and locations (Fig. 4g-i5e, f, i), highlighting the numerical dominance of small particles in the study area.

The distribution of PVC along the three transects in the study area, as well as the proportions of small and large particles contributing to PVC, are shown in Fig. 5. Particle volume concentration (PVC) ranged from 0 to 6.7 mm³ L⁻¹, with a mean of 0.3 ± 0.4 mm³ L⁻¹ (mean ± SD) in this study. Overall, high PVC values in the study area were primarily observed in the upper water column, while values decreased markedly as water depth increased (Fig. 5a-c). In waters shallower than 200 m, the mean PVC was 0.4 ± 0.7 mm³ L⁻¹ (mean ± SD), which was significantly higher than that in waters deeper than 200 m, where the mean PVC was 0.2 ± 0.1 mm³ L⁻¹ (mean ± SD) (*t*-test, *p* < 0.01). The overall distribution of PVC across the three transects generally aligns with the patterns observed in particle abundance but exhibits some notable differences (Fig. 6). In Transect 1, PVC was highest at the inner slope station S1 and progressively decreased toward the outer slope stations (Fig. 56a). A similar pattern was observed in Transect 2, where PVC was elevated at the inner slope station S8, followed by a gradual decline toward the outer slope (Fig. 5b6d). In Transect 3, PVC was relatively high in the upper layers 70 m at the outermost stations S11 and S12, with concentrations decreasing with depth (Fig. 5c6e). An increase in PVC was observed in the mesopelagic layer (300–600 m) at station S12. Notably, despite the high particle abundance observed in the deep waters at stations S2 and S10, PVC in these layers remained low (Fig. 6a, g). This discrepancy suggests that the high particle abundance in these regions was primarily driven by small particles, which contributed minimally to the overall particle volume. In contrast, at stations S11 and S12, the PVC distribution closely followed the particle abundance pattern, with elevated concentrations reaching up to 1.2 mm³ L⁻¹ in the upper water column. Representative particle images captured by the UVP in the upper layers at stations S11 and S12 are shown in Fig. 7.

For the whole study region, small particles contribute between 13% and 74% (mean ± SD: =39% ± 12%) of the total PVC (Fig. 5d-f), while large particles account for 26% to 87% (mean ± SD: =61% ± 12%) (Fig. 5g-i). For small particles, their contribution to PVC was generally around 40%–50% across most areas (Fig. 5d-f). However, notable variations were observed in certain regions. At station S2 on transect 1, a sharp increase occurred

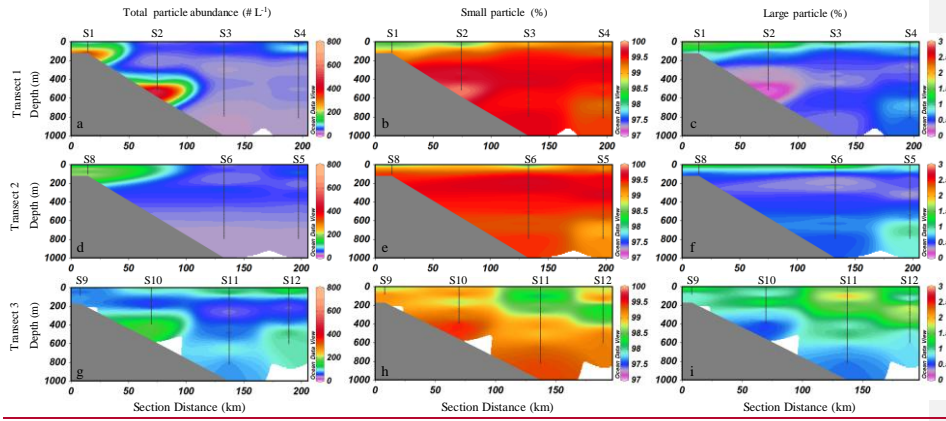
带格式的: 字体: Times New Roman

420 in the bottom layer around 500 m depth, where the proportion exceeded 60% (Fig. 5d). In contrast, at stations S11 and S12 on transect 3, a marked decrease was observed in the upper to mid-depth layers, particularly above 400 m, where the proportion dropped to 30% or even lower (Fig. 5f). Large particles exhibited an opposite distribution pattern in their contribution to PVC (Fig. 5g-i). Unlike their overwhelming dominance in particle abundance, small particles no longer play a predominant role in PVC. Instead, large particles contribute a greater proportion to PVC, emphasizing their larger size and greater volumetric influence despite their low numerical abundance.

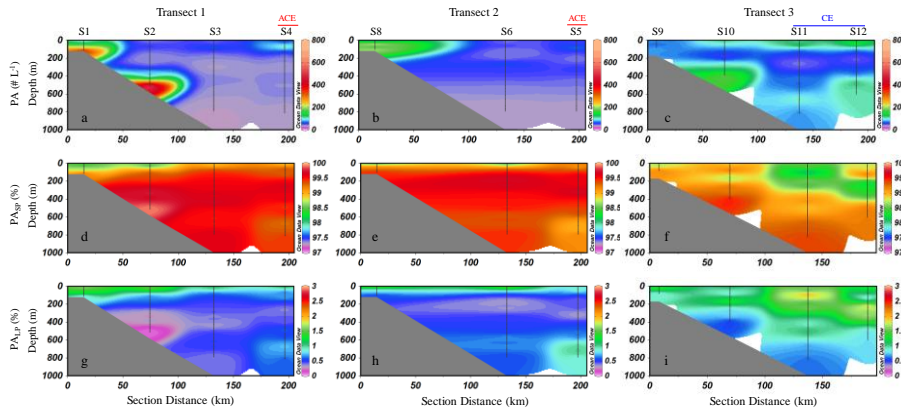
425 Particle abundance and PVC showed clear spatial differences between the cyclonic and anticyclonic eddy regions (Fig. S3). At the anticyclonic eddy stations (S4 and S5), particle abundance remained low in the upper 50 m layer, averaging 51 particles L^{-1} , and PVC values were also limited, generally less than $0.3 \text{ mm}^3 L^{-1}$. In contrast, the cyclonic eddy stations (S11 and S12) exhibited significantly higher values for both parameters. Particle abundance at these stations exceeded 120 particles L^{-1} , and PVC increased markedly under the influence of cyclonic eddies, with values exceeding $0.6 \text{ mm}^3 L^{-1}$. Figure 6 shows the PVC values at different depths and the percentage contributions of small and large particles at stations influenced by anticyclonic eddies (S4, S5) and cyclonic eddies (S11, S12). Notable differences in PVC values and particle size composition can be observed
430 between these two regions. At nearly all depth, PVC at S11 and S12 is higher than at S4 and S5 (Fig. 6a). At S4 and S5, small particles contribute more than 40% to PVC across all depths, except at 200 m at S4, while large particles contribute less than 60% (Fig. 6b, c). In contrast, at S11 and S12, the contribution of small particles is generally less than 40% at most depths, particularly above 500 m, whereas large particles contribute more than 60% (Fig. 6d, e). The proportion of large particles at S11 and S12 is higher than at S4 and S5.

435

436



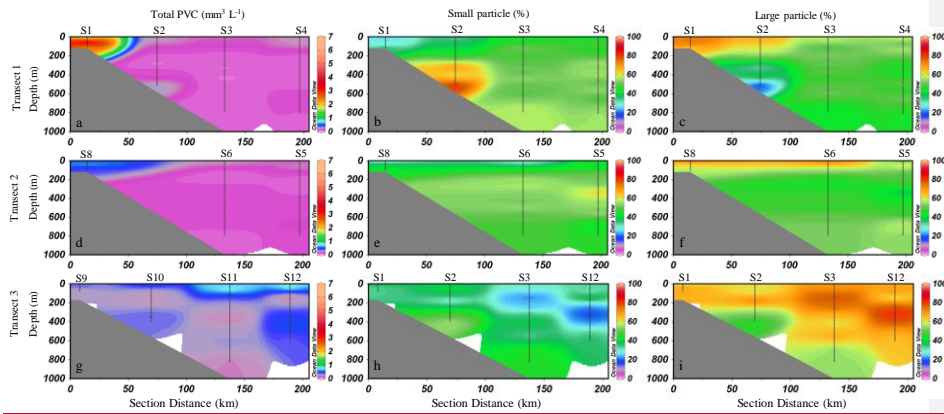
437



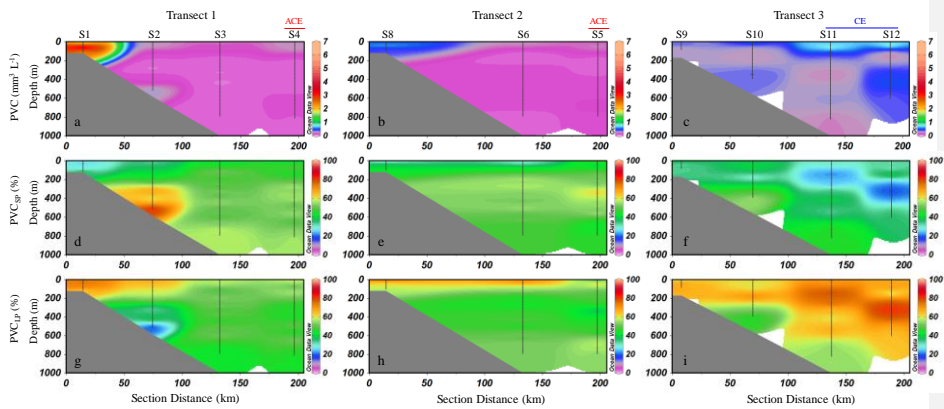
438 **Fig. 4** Vertical distribution of particles abundance ($PA, \# L^{-1}$) and the relative proportion of small particles (PA_{SP}, ESD
 439 $< 500 \mu m$) and large particles ($PA_{LP}, ESD \geq 500 \mu m$) within the total particle abundance. PA : a-c; $PA_{SP}\%$: d-f;
 440 $PA_{LP}\%$: g-i. SP : small particles; LP : large particles. ACE represents stations influenced by anticyclonic eddies, while
 441 CE represents stations influenced by cyclonic eddies.

442 **Fig. 5.** Vertical distribution of particles abundance ($\# L^{-1}$) and the relative proportion of small particles ($ESD < 500$
 443 μm) and large particles ($ESD \geq 500 \mu m$) within the total particle abundance. **Transect 1:** particle abundance (a, $\# L^{-1}$),
 444 small particles (%) (b), large particles (%) (c); **Transect 2:** particle abundance (d, $\# L^{-1}$), small particles (%) (e), large
 445 particles (%) (f); **Transect 3:** particle abundance (g, $\# L^{-1}$), small particles (%) (h), large particles (%) (i)

带格式的：字体：小五，加粗



446



447

448 **Fig. 56. Vertical distribution of particle volume concentration (PVC) ($\text{mm}^3 \text{L}^{-1}$) along the three transects and the**
 449 **percentage contributions of small and large particles. PVC: a-c: percentage of small particles; d-f: percentage of large**
 450 **particles; g-i. SP: small particles; LP: large particles. ACE represents stations influenced by anticyclonic eddies, while**
 451 **CE represents stations influenced by cyclonic eddies, and the relative contribution of small particles ($\text{ESD} < 500 \mu\text{m}$)**
 452 **and large particles ($\text{ESD} \geq 500 \mu\text{m}$) to the total PVC. Transect 1: PVC (a , $\text{mm}^3 \text{L}^{-1}$), small particles (%) (b), large**
 453 **particles (%) (c); Transect 2: PVC (d , $\text{mm}^3 \text{L}^{-1}$), small particles (%) (e), large particles (%) (f); Transect 3: PVC (g ,**
 454 **$\text{mm}^3 \text{L}^{-1}$), small particles (%) (h), large particles (%) (i)**

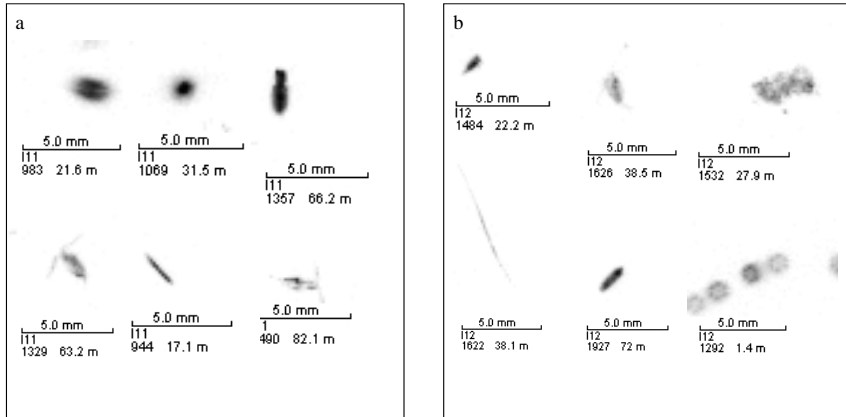


Fig. 7. Representative images of large particles captured by the UVP at station S11 and S12. a: S11; b: S12. Scale bar represents 5 mm. Each image includes the station name, image number, and the depth at which it was taken.

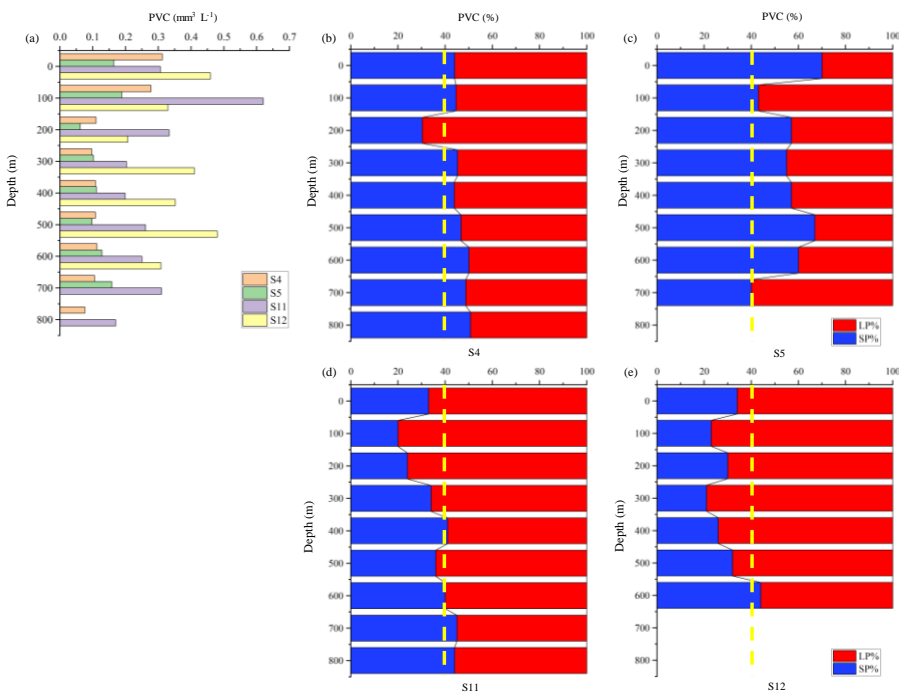


Fig. 6. PVC ($\text{mm}^3 \text{L}^{-1}$) at different depths at stations influenced by anticyclonic eddies (S4, S5) and cyclonic eddies (S11, S12) (a), along with the percentage contributions of small and large particles to PVC at each station (b-d).

Vertically, the mean particle abundance and PVC in waters shallower than 200 m were 79 ± 70 particles L^{-1} and $0.4 \pm 0.7 \text{ mm}^3 \text{L}^{-1}$, respectively, which were significantly higher than those in waters deeper than 200 m, with mean values of 59 ± 66 particles L^{-1} and $0.2 \pm 0.1 \text{ mm}^3 \text{L}^{-1}$ (t -test, $p < 0.01$) (Supplementary Fig.-S4). This indicates that, overall, particle abundance and PVC are higher in the upper 200 m zone compared to deeper waters.

465

3.3 POC export flux and spatial variability

The POC export flux, derived from UVP-based particle size distributions, exhibited a wide range from 3.4 to 302.4 mg C m⁻² d⁻¹, with a mean value of 33.6 ± 34.9 mg C m⁻² d⁻¹ across the study area. Overall, high POC fluxes in the study area were primarily concentrated in the upper 200 m, while fluxes below 200 m were substantially lower (Fig. 7). Notable spatial heterogeneity was observed both within and between transects (Fig. 8), reflecting the combined influence of productivity gradients, hydrodynamic structure, and particle aggregation dynamics. In Transect 1, the highest fluxes were concentrated at the nearshore station S1, particularly within the 50–70 m depth range, where values peaked at 302.0 mg C m⁻² d⁻¹ (Fig. 87a). In contrast, offshore stations along the same transect displayed significantly lower fluxes, generally below 40 mg C m⁻² d⁻¹, indicating a strong coastal-to-offshore decline driven by reduced primary production and weaker aggregation processes. A similar nearshore-to-offshore gradient was observed in Transect 2, where the maximum flux (164.0 mg C m⁻² d⁻¹) was recorded at 40 m depth at station S8, gradually decreasing toward deeper slope stations (Fig. 87b). Transect 3 showed a distinct pattern, with elevated POC fluxes occurring at offshore stations S11 and S12 (Fig. 87c). At station S11, the highest flux (212 mg C m⁻² d⁻¹) was recorded at 60 m, while at station S12, the flux peaked at 210 mg C m⁻² d⁻¹ at 40 m. Moreover, POC fluxes at depths of 200–600 m at stations S11 and S12 remained substantially higher than those at comparable depths in the offshore stations of Transects 1 and 2 (Fig. 8a, b), implying sustained vertical transfer of organic material.

The contribution of small and large particles to POC flux across the study area was shown in Supplementary Fig. S3. Small particle-derived carbon flux accounted for 5% to 77% of the total POC flux, with an average contribution of 24% ± 12%, while large particle-derived carbon flux ranged from 23% to 95%, averaging 76% ± 12%. The contribution of large particles to the POC flux was significantly higher than that of small particles (*t*-test, *p* < 0.05). Vertically, in waters shallower than 200 m, small particles contributed 19 ± 9% to the POC flux (mean ± SD), while large particles accounted for 81 ± 9%. In contrast, below 200 m, the contribution of small particles increased to 28 ± 12%, with large particles contributing 72 ± 12%. The contribution of small particles to POC flux below 200 m was significantly higher than that in the upper 200 m (*t*-test, *p* < 0.05).

490

带格式的: 字体: Times New Roman

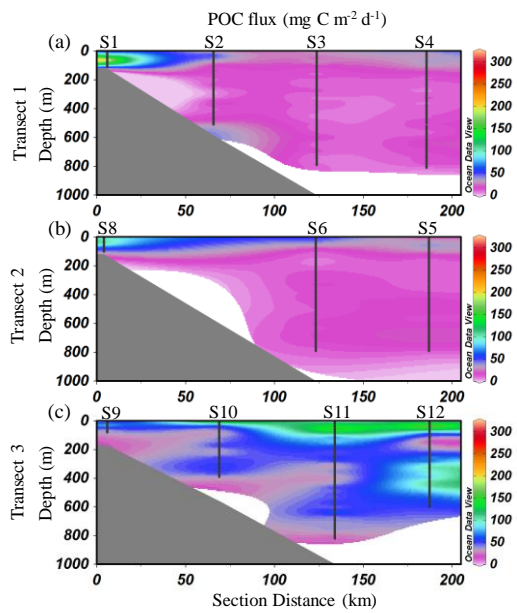
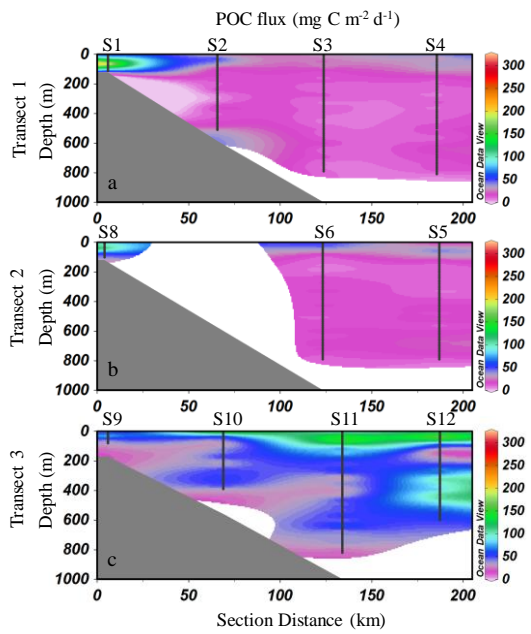
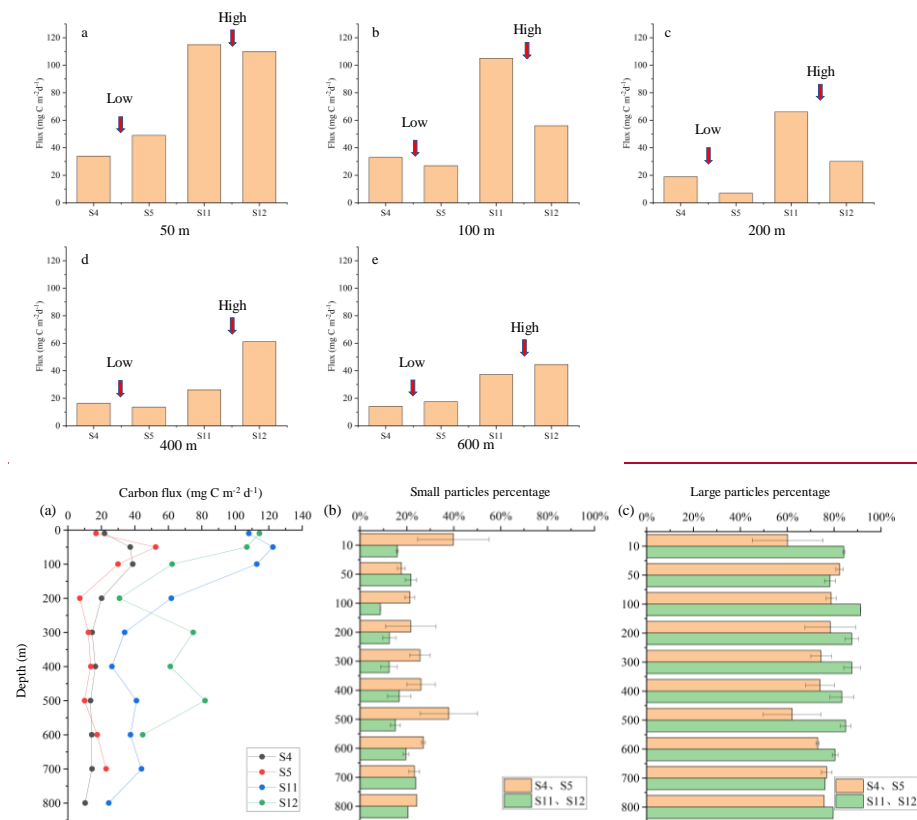


Fig. 78 Vertical distribution of POC flux across the three transects (mg C m⁻² d⁻¹) in the study area. a: Transect 1; b: Transect 2; c: Transect 3

The POC flux patterns differed markedly between stations influenced by anticyclonic eddies (S4, S5) and

500 cyclonic eddies (S11, S12) (Fig. 8). In terms of flux magnitude, the highest values at all stations were observed above 100 m. However, POC fluxes at S11 and S12 were consistently higher than those at S4 and S5 across all depths (Fig. 8a). Regarding flux composition, the contribution of small particles to the POC flux was generally higher at the anticyclonic eddy-influenced stations S4 and S5 than at the cyclonic eddy-influenced stations S11 and S12 (Fig. 8b), whereas the contribution of large particles was greater at S11 and S12 compared to S4 and S5 (Fig. 8c). POC fluxes exhibited pronounced spatial and vertical variability between the cyclonic-eddy-influenced and anticyclonic-eddy-influenced regions (Fig. 9). At the upper layers (50 m and 100 m), POC fluxes were substantially higher at the cyclonic-eddy stations (S11 and S12), with maximum values exceeding $100 \text{ mg C m}^{-2} \text{ d}^{-1}$. In contrast, the anticyclonic-eddy stations (S4 and S5) exhibited much lower fluxes, generally below $60 \text{ mg C m}^{-2} \text{ d}^{-1}$ (Fig. 9a, b). At 200 m, this pattern persisted, with S11 maintaining the highest flux, while S4 and S5 showed sharp decreases to below $30 \text{ mg C m}^{-2} \text{ d}^{-1}$, indicating limited vertical export in the anticyclonic eddy region (Fig. 9c). Deeper layers (400 m and 600 m) also demonstrated elevated fluxes at the cyclonic-eddy stations, especially S12, where fluxes remained above $60 \text{ mg C m}^{-2} \text{ d}^{-1}$. Meanwhile, fluxes at S4 and S5 were consistently low across all depths, with values typically below $30 \text{ mg C m}^{-2} \text{ d}^{-1}$ (Fig. 9d, e).



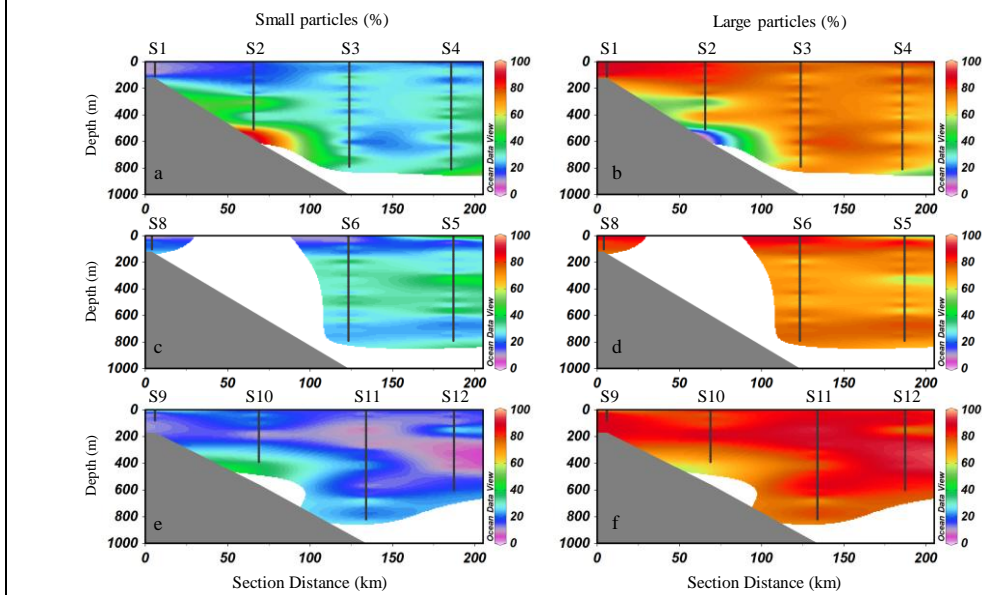
510 **Fig. 89** POC flux derived from UVP data in different water layers and contributions of small and large particles at stations located in the anticyclonic eddy region (S4, S5) and cyclonic eddy region (S11, S12). a: 50 m; b: 100 m; c: 200-

515 m; d: 400 m; e: 600 m. a: Carbon flux ($\text{mg C m}^{-2} \text{d}^{-1}$); b: Small particles percentage; c: Large particles percentage.

S4, S5: the average values of stations S4 and S5; S11, S12: the average values of stations S11 and S12.

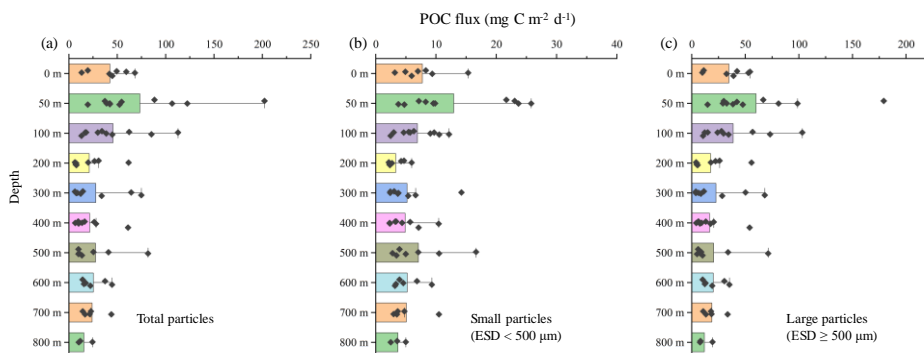
带格式的: 字体: Times New Roman

520 The contribution of small and large particles to POC flux exhibits considerable variability across the study area (Fig. 10). Small particle-derived carbon flux accounted for 5.1% to 76.7% of the total POC flux, with an average contribution of $23.8\% \pm 11.5\%$, while large particle-derived carbon flux ranged from 23.3% to 95.0%, averaging $76.2\% \pm 11.5\%$. A few exceptions are noteworthy. At 500 m depth at station S2, small particles contributed more than 50% of the POC flux (Fig. 10a), while at 380 m depth at station S10, small particles accounted for over 30% of the POC flux (Fig. 10e), higher than in other regions. In contrast, in the 200–600 m depth range at stations S11 and S12, the contribution of large particles to POC flux increased, with an average proportion of 87% (Fig. 10f). This proportion was notably higher than that in the same depth range at the offshore stations of Transects 1 and 2, where large particles accounted for 71% and 68% of the POC flux, respectively (Fig. 10b, d). The increased dominance of large particles at depth in Transect 3 suggests more efficient transport of larger aggregates, potentially influenced by mesoscale eddies or enhanced particle formation and retention processes.



530 **Fig. 10 Contribution of small and large particles to the POC flux across the three transects in the study area.**
Transect 1: a, small particles (%); b, large particles (%). Transect 2: c, small particles (%); d, large particles (%).
Transect 3: e, small particles (%); f, large particles (%).

535 Vertically, high POC export flux values are predominantly observed within the upper 100 m, with peak concentrations around the 50 m depth layer (Fig. 11a). Below 100 m, the flux generally exhibits a decreasing trend with increasing depth. This pattern is consistent for both small and large particles, as their respective carbon flux distributions follow a similar trend (Fig. 11b, c). However, the percentage contributions of small and large particles to the total POC flux exhibited distinct vertical patterns. Specifically, the relative contribution of small particles generally increased with depth, while that of large particles showed a decreasing trend (Supplementary Fig. S5).



540 **Fig. 11 Vertical distributions of POC export flux ($\text{mg C m}^{-2} \text{d}^{-1}$) in different layers in the study area. a: total POC export flux; b: export flux of small particles ($\text{ESD} < 500 \mu\text{m}$); c: export flux of large particles ($\text{ESD} \geq 500 \mu\text{m}$). Box plots show the median value (mid-line), the 25% and 75% quantiles (box), and the 5 and 95% quantiles (whiskers).**

545 **3.4 Correlation analysis**

The results of the PearsonCA correlation analysis indicate that above 200 m, POC flux does not exhibit significant correlations with most environmental factors in the upper 200 m layer, except for water depth and Chl *a* concentration (Fig. 129a). POC flux shows a significant negative correlation with water depth and a significant positive correlation with Chl *a* concentration. In addition to the correlation matrix, scatter plot analyses further revealed significant positive relationships between POC flux at 200 m, 400 m, and 600 m depths and the water-column integrated Chl *a* concentrations above 200 m (Fig. 9b+2b-d). For the 400 m and 600 m depth layers, the POC flux showed no significant correlation with the integrated Chl *a* concentration in the upper 200m of the water column (Fig. 9c, d). The strength of correlation remained consistent across these depth layers, indicating that surface phytoplankton biomass is a key determinant of vertical carbon flux throughout the upper to mid-mesopelagic zone. These results suggest a tight coupling between surface production and deep particle export. Scatter plot analysis across the full water column revealed contrasting relationships between POC flux and the abundance of small and large particles (Fig. 13). No significant correlation was found between POC flux and small particles (Fig. 13a), suggesting that variations in the abundance of small particles alone are not reliable indicators of vertical carbon export. In contrast, POC flux showed a significant positive linear correlation with large particle abundance (Fig. 13b), with a fitted regression equation of $y = 48.63x - 3.27$ ($p < 0.05$). This pattern underscores the dominant role of large particles in mediating efficient vertical carbon transfer.

550

555

560

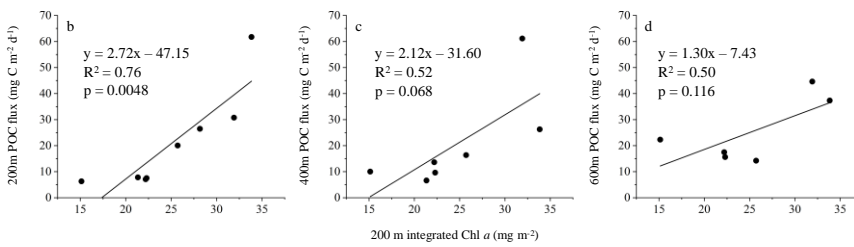
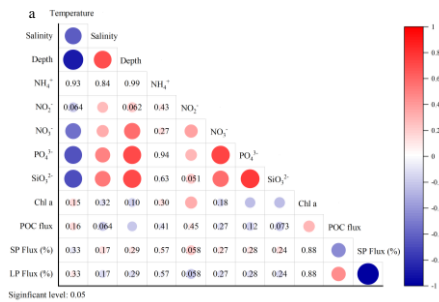
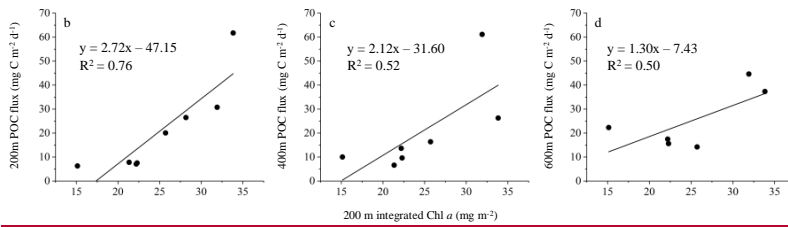
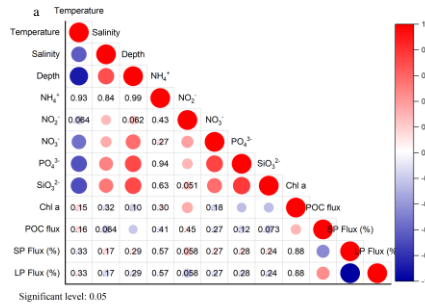


Fig. 912 Correlation analysis between POC flux and environmental factors.

a: Heatmap showing of Pearson r correlation coefficients (r) Analysis between POC flux and environmental variables in the upper 200 m and environmental factors; Significant correlations ($p < 0.05$) are highlighted by filled circles with color intensity proportional to r , but the correlation coefficient values are not labeled. Non-significant correlations ($p \geq 0.05$) are indicated by numeric r values only. **b-d:** Correlation between POC (mg C m⁻² d⁻¹) flux at 200 m, 400 m, and 600 m depth and the integrated Chl a concentration (mg m⁻²) in the upper 200m. SP: small

带格式的: 字体: Times New Roman

particle; LP: large particle. A significance level of $p < 0.05$ was used to determine statistical significance.

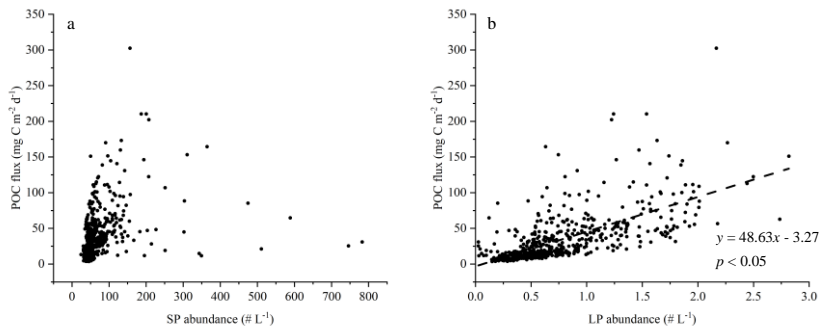


Fig. 13 Scatter plots of POC flux versus abundance of small particles (a) and large particles (b). SP: small particle; LP: large particle. p represents the PCA correlation coefficient, and $p < 0.05$ indicates a significant correlation between the two datasets.

4 Discussion

4.1 Marine particle distribution and controls: cross-system comparisons and regional characteristics

Comparison of particle abundance and volume concentration with other oceanic regions

The particle abundance and volume concentration (PVC) observed with UVP along the continental slope of the SCS in this study offer important context for understanding regional particle dynamics. Compared to traditional methods such as sediment traps and bottle sampling, which often suffer from low spatial resolution and potential particle alteration during collection (Buesseler-Ramondene et al., 200746), the UVP provides continuous, high-resolution *in situ* imaging of marine particles. It enables detailed quantification of particle abundance, size distribution, and volume concentration across the entire water column with minimal disturbance, offering new insights into particle-mediated carbon export processes in this area. When compared to UVP data from other oligotrophic oceanic regions, our findings fall within the broad range of particle concentrations and volume reported for similar low-nutrient systems (Table 2), oligotrophic to mesotrophic systems. This comparison while also highlights the role of environmental variability in shaping particle distributions in the oligotrophic SCS (Table 2). The particle abundance in the SCS continental slope (0–100 m: 25–476 particles L⁻¹; 0–800 m: 0–783 particles L⁻¹, mean \pm SD: 68 ± 69 particles L⁻¹) is comparable to values reported for oligotrophic regions such as the High Nutrient, Low Chlorophyll (HNLC) areas of the Southern Ocean observations in regions like the HNLC (High Nutrient, Low Chlorophyll) stations of the Southern Ocean (0–100 m: 0–500 particles L⁻¹; Jouandet et al., 2011), and markedly higher than those observed in the mesopelagic zone (200–1000 m) of the Equatorial Pacific mesopelagic zone (1–4 particles L⁻¹; Pretty, 2019). However, it is notably lower than the particle abundance during an iron-fertilized bloom station in the Southern Ocean (1400 ± 200 particles L⁻¹; Jouandet et al., 2011), where artificial nutrient enrichment significantly boosted particle production. This discrepancy underscores the influence of localized biogeochemical conditions on particle abundance. In terms of particle volume concentration (PVC), the SCS continental slope exhibits values ranging from 0–6.7 mm³ L⁻¹ (mean \pm SD: 0.3 ± 0.4 mm³ L⁻¹), aligning well with the Gulf of Alaska shelf (0.1–1 mm³ L⁻¹; Turner et al., 2017) and the HNLC stations in the

Southern Ocean ($0\text{--}50 \text{ mm}^3 \text{ L}^{-1}$; Jouandet et al., 2011). Conversely, these values are lower compared to the iron-fertilized bloom stations ($183 \pm 34 \text{ mm}^3 \text{ L}^{-1}$; Jouandet et al., 2011), reflecting the significant impact of primary production and aggregation processes. ~~Overall, the particle abundance and volume concentration observed in this study are consistent with those from other oligotrophic and mesotrophic regions.~~ The differences between regions ~~suggest~~highlight the importance of local environmental factors, including nutrient availability, primary production, and physical oceanographic conditions, in shaping marine particle dynamics.

605

608 Table 2 Comparison of particle abundances and volume concentrations in this study with those in other studies. —:
 609 no data. Data from the upper 100 m layer are presented separately to facilitate comparison with previous studies
 610 using similar sampling depths (e.g., Iversen et al., 2010; Jouandet et al., 2011).

Location	Depth (m)	Particle abundance range (mean±SD) (# L ⁻¹)	PVC range (mean±SD) (mm ³ L ⁻¹)	Reference
The North Mediterranean	0–400	0–80	—	Gorsky et al., 2000
The Ligurian Sea	0–1000	0–1108	—	Stemmann et al., 2008
Off Cape Blanc, NW Africa	0–80	30–100	—	Iversen et al., 2010
The HNLC stations in the Southern Ocean	0–100	0–500	0–50	Jouandet et al., 2011
Iron-fertilized bloom station in the Southern Ocean	0–100	1400 ± 200	183 ± 34	Jouandet et al., 2011
Southeast of Kerguelen Island (Southern Ocean)	0–100	90 ± 5	0.3 ± 0.1	Jouandet et al., 2014
The Gulf of Alaska shelf	0–40	—	0.1–1	Turner et al., 2017
The Equatorial Pacific	200–1000	1–4	—	Pretty 2019
The North Pacific Gyre	>1000	0.1–0.3	—	Pretty 2019
The eastern tropical North Pacific	160–500	1–10	—	Cram et al., 2022
Station ALOHA (22.75°N, 158.00°W)	0–75	50–125	—	James 2024
SCS	0–100	25–476 (95 ± 71)	0.0–6.7 (0.6 ± 0.8)	This study
SCS eontinental slope	0–800	0–783 (68 ± 69)	0.0–6.7 (0.3 ± 0.4)	This study

带格式的: 字体: Times New Roman

611

4.2 Distribution characteristics and influencing factors of marine particles

Horizontally, particle abundance and PVC exhibited clear cross-shelf gradients, with higher values observed at the inner slope stations, and a decreasing trend toward offshore waters (Fig. 4a-c5a-d; Fig. 5a-c6a-d). This pattern is consistent with observations from several other oceanic regions. This nearshore to offshore decline is consistent with previous findings. Guidi et al. (2008) studied the distribution of particles ($>100 \mu\text{m}$) in the South-Eastern Pacific, and found that particle concentrations were highest over the Peru-Chile continental shelf, and decreased progressively toward the open ocean. Forest et al. (2012) found that particle abundance and volume in the surface layer of southeast Beauford Sea exhibited a decline of approximately two orders of magnitude when progressing from the shelf toward the basin in July-August 2009. This cross-shelf trend was primarily attributed to the spatial distribution of Chl *a*. Turner et al. (2017) measured the concentrations of marine particles in the Gulf of Alaska during summer 2015, and found that particle concentrations were highest at stations closest to large inputs of freshwater and glacial discharge, intermediate at some nearshore stations and at the shelf break, and lowest over the mid-shelf. Therefore, our results, in line with previous studies, indicate that particle concentrations tend to be higher in nearshore regions, reported a two-order-of-magnitude drop in large particle abundance from the shelf to the basin across the Mackenzie shelf (Arctic Ocean), while Turner et al. (2017) observed the highest particle concentrations near freshwater-influenced shelf breaks in the Gulf of Alaska, decreasing over mid-shelf regions. In this study, it was observed that the depth of the nutricline at inner slope stations was shallower than that at outer slope stations (Fig. 3). In the present study, the shallow nutricline observed at inner slope stations could (Fig. 3a-d) enhance light availability in the SCM layer, likely promoting higher Chl *a* concentrations (Fig. 4a-b). The distribution of Chl *a* also clearly indicates that the DCM layer at inner slope stations exhibited higher Chl *a* concentrations compared to outer slope stations (Fig. 3j-l). The resulting increase in phytoplankton biomass may stimulate organic matter production and particle aggregation (Panaïotis et al., 2024), thereby contributing to elevated particle concentrations there. Additionally, nearshore regions are more susceptible to terrestrial inputs. On one hand, riverine input can supply nutrients, stimulating primary productivity and particle formation (Turner et al., 2017). The elevated surface nutrient and Chl *a* concentrations observed at station S9 in this study provide direct evidence of this process (Fig. 3c, j). On the other hand, the proximity to the continental margin increases exposure to lithogenic inputs from terrestrial sources (Liu et al., 2016), further enhancing particle loads in inner slope waters. Therefore, from a horizontal perspective, the combined influence of terrestrial inputs and a shallower nutricline in inner shelf regions enhances biogeochemical processes that lead to higher particle concentrations compared to outer slope areas.

In addition to identifying patterns of particle distribution in the SCS slope that are consistent with observations from other oceanic regions, we also observed several localized and unique features specific to this region. In contrast, the most notable one is the elevated particle abundances and PVC observed at stations S11 and S12 along Transect 3 (Fig. 4c, Fig. 5c). At stations S11 and S12, surface particle abundance and PVC reached as high as $130 \text{ particles L}^{-1}$ and $0.45 \text{ mm}^3 \text{ L}^{-1}$, respectively, substantially higher than those observed at the inner slope station S9, which recorded $80 \text{ particles L}^{-1}$ and $0.18 \text{ mm}^3 \text{ L}^{-1}$. Given their offshore location ($> 200 \text{ km}$ from land), the particle enrichment at these sites (S11 and S12) is unlikely to stem from terrestrial inputs and instead reflects localized biological production. Transect 3 exhibited elevated particle abundance and PVC in the upper water column at offshore stations S11 and S12 (Fig. 5g; Fig. 6g). Sea level anomaly (SLA) data revealed that these stations were positioned at the periphery of a cyclonic eddy located to their northeast (Fig. 1d). Given their offshore

带格式的: 字体: Times New Roman

location (>200 km from land), the particle enrichment at these sites is unlikely to stem from terrestrial inputs and instead reflects localized biological production. Mesoscale eddies are known to influence upper-ocean nutrient supply, productivity levels, and the physical structure of the water column modulate particle dynamics through their effect on nutrient entrainment, biological productivity, and physical retention (Maiti et al., 2008). Cyclonic eddies, in particular, induce upward vertical transport that enhances nutrient supply to the euphotic zone, stimulating phytoplankton growth and aggregate formation (Kahru et al., 2007). Furthermore, convergence and retention zones along the eddy periphery can trap suspended and sinking particles, facilitating localized particle accumulation (Accardo et al., 2025). In our study, the elevated particle concentrations at S11 and S12 support this mechanism (Fig. 5), suggesting a coupling between eddy-driven nutrient enhancement and biological particle production. UVP imagery also revealed that large phytoplankton cells and zooplankton dominated the particle assemblages at these sites (Fig. 7), reinforcing the biological origin of the observed signal.

Another localized and distinct observation was the exceptionally high particle abundance detected in the bottom layers at stations S2 and S10 (Fig. 4a, c). Specifically, particle abundance reached 746 particles L^{-1} at 500 m at station S2 and 214 particles L^{-1} at 390 m at station S10. These values were substantially higher than those observed in the surface layers at the same stations, which recorded only 25 and 135 particles L^{-1} , respectively. However, based on the distribution of PVC, no significant particle enrichment was observed at these two stations (Fig. 5a, c). At the bottom layer at these two stations, the particle population was overwhelmingly dominated by small particles, which accounted for more than 99.8% of the total abundance (Fig. 4d, f). This explains why the exceptionally high particle numbers did not correspond to elevated PVC values there. At mid-slope stations S2 and S10, anomalously high particle abundance was detected in the deep water column (Fig. 5a, g). However, these elevated concentrations were primarily composed of small particles, resulting in no corresponding increase in PVC (Fig. 6a, g). Given the low particle concentrations observed in the upper water column at these two stations, it is unlikely that the elevated particle abundance in the bottom layer resulted from vertical settling from above. This particle size structure suggests that the deep-layer signal reflects fine suspended material rather than rapidly sinking aggregates. One plausible explanation for this deep particle enrichment is the presence of intermediate nepheloid layers (INLs). INLs are formed by suspended particles spreading along isopycnal surfaces and are commonly found near the edges of continental shelves, slopes, and seamounts (Oliveira et al., 2002). In the SCS, they are primarily formed as a result of which form due to resuspension and lateral transport of fine particles along the continental slope (Chen et al., 2024). These layers are often associated with bottom boundary layer dynamics or internal waves, which can enhance the lateral advection of resuspended material from the continental margin into the deep slope region (Jia et al., 2019). The composition of INLs typically consists of a mixture of fine-grained lithogenic particles, resuspended sediments, and biogenic detritus (Oliveira et al., 2002). In this study, small particles could not be imaged, and thus their composition remains unknown. However, the low abundance of large zooplankton observed in this area (Supplementary Fig. S2a, c) does not support the presence of substantial amount of living particles in the bottom layer. The exceptionally high particle abundance observed here is more likely derived from sediment resuspension rather than from vertical export originating in the upper euphotic layer.

Both particle abundance and PVC in the study area showed a decreasing trend with increasing depth. Waters shallower than 200 m exhibited significantly higher particle abundance and PVC compared to deeper waters (Supplementary Fig. S4). Although elevated particle abundance was observed in the deep layers at station S2 and S10, their corresponding PVC values remained relatively low (Fig. 5, 6), indicating a predominance of small-sized particles at these depths. The decrease in particle concentration from 0 – 200 m to 200 – 800 m water depth on the

695 SCS continental slope highlights distinct vertical processes influencing particle dynamics in this region. The
elevated particle concentrations in the upper 200 m can primarily be attributed to biological production in the
euphotic zone, where photosynthetic activity by phytoplankton dominates (Fig. 4). This process could generate
abundant organic matter, including individual cells, aggregates, and detritus, which constitute a significant portion
of the observed particles (Panaiotis et al., 2024). Additionally, processes such as grazing by zooplankton,
700 production of fecal pellets, and aggregation further contribute to particle abundance in the upper water column
(Fender et al., 2019). In contrast, the lower particle concentrations in the 200–800 m depth range reflect the
combined effects of particle export, degradation, and remineralization during vertical transport. As particle sink, a
substantial portion undergoes biological consumption by heterotrophic organisms or is remineralized into
dissolved organic matter (Guidi et al., 2008b; Turner, 2015). Furthermore, smaller particles, which dominate in
size below the euphotic zone, are more susceptible to disaggregation with slower sinking rates (Durkin et al., 2015).
705 These observations align with global trends, where particle concentrations typically decrease with depth, driven
by the attenuation of biological and physical processes (Kiko et al., 2022). The pronounced vertical particle
concentration gradient underscores the efficiency of biological and microbial processes in the upper mesopelagic
zone, which mediate the transfer and transformation of organic carbon.

4.3 Implications for carbon export and comparisons between large and small particles

4.2 Numerical dominance of small particles vs. biogeochemical significance of large particles

710 The size composition of marine particles is critically important, as it governs their sinking efficiency, with
smaller particles typically sinking much more slowly than larger ones (Clements et al., 2023). In addition, vertical
variations in particle size composition can offer insights into particle degradation and transformation processes
occurring within the water column (Cram et al., 2022). Using data from the UVP, this study characterizes the size
composition of marine particles along the SCS slope. Small particles contributed over 98% to the total particle
715 abundance in most areas (Fig. 4d-f), highlighting their overwhelming numerical dominance. Slight decreases in
the relative contribution of small particles were only observed in certain high-productivity regions, such as the
nearshore stations of Transects 1 and 2, and stations S11 and S12 along Transect 3. Due to the lack of image data
for small particles, we were unable to determine the exact cause of the decreased proportion of small particles in
these areas. The notably elevated zooplankton abundance observed at these stations suggests that zooplankton
720 activity may be a contributing factor (Supplementary Fig. S2a-c). Overall, the study area represents a typically
oligotrophic environment. Previous studies have reported low phytoplankton productivity in this region, with the
community largely dominated by picophytoplankton (Zhang et al., 2023). The low biomass and small size of
phytoplankton cells limit their ability to form large particles or aggregates through aggregation processes.
725 Additionally, low primary productivity is often accompanied by low large zooplankton abundance (Liu et al., 2020).
This pattern contrasts with nearshore or high-productivity regions. For instance, Stemmann et al. (2008) observed
that in coastal and frontal zones of the northwestern Mediterranean, phytoplankton aggregation can lead to the
formation of large particles, thereby increasing the relative contribution of the larger size classes.

730 The POC export flux estimated from the UVP-derived particle size distribution in the SCS continental slope
ranged from 3.4 to 302.4 mg C m⁻² d⁻¹, with an average of 33.6 mg C m⁻² d⁻¹ in this study. These values are broadly
consistent with previous estimates using independent methodologies in the SCS. For instance, Cai et al. (2015)
reported POC export fluxes at 100 m depth in the northern slope of the SCS based on ²³⁴Th/²³⁸U disequilibrium,

735 ranging from 24.0 to 76.8 mg C m⁻² d⁻¹. Similarly, Zhang et al. (2020) estimated POC export fluxes of 20.3 ± 2.2
mg C m⁻² d⁻¹ at 120 m depth in the core of an anticyclonic eddy in the SCS slope region. The agreement between
these independent measurements suggests that UVP-based approaches provide a reasonable information of POC
740 export fluxes in the SCS continental margin. Our results also align with UVP-based POC flux estimates in other
oceanic regions. For example, Ramondene et al. (2016) reported a wide range of POC export fluxes in the
Mediterranean Sea, spanning 0 to 504 mg C m⁻² d⁻¹, while Fender et al. (2019) documented an average flux of 42.1
mg C m⁻² d⁻¹ in the California Current Ecosystem. These comparisons highlight the applicability of UVP-based
particle flux estimations across diverse oceanic settings.

745 Although small particles overwhelmingly dominated in terms of abundance, the pattern was notably different
when PVC was considered. Across the entire study area, small particles contributed between 13% and 74% of the
total PVC (mean ± SD: 39% ± 12%) (Fig. 5d-f), whereas large particles accounted for a substantially higher
share, ranging from 26% to 87% (mean ± SD: 61% ± 12%) (Fig. 5g-i). This contrast became even more pronounced
when examining carbon fluxes. Small particle-derived POC flux accounted for 5% to 77% of the total, with an
average contribution of 24% ± 12%, whereas large particles contributed the majority of carbon export, ranging
750 from 23% to 95%, with a mean of 76% ± 12% (Supplementary Fig. S3). The UVP data reveal a clear dominance
of small particles (ESD < 0.5 mm) in terms of abundance throughout the water column, accounting for over 97%
of total particle abundance (Fig. 5). However, when examining volume concentration, a contrasting pattern
emerges: small particles contribute a lower proportion to the total particle volume compared to large particles
(ESD ≥ 0.5 mm) (Fig. 6). Specifically, in the 0–200 m layer, large particles account for an average of 61% of the
total volume, whereas small particles contribute only 39%. This trend shifts slightly in deeper waters (>200 m),
where the contribution of large particles decreases to 52%, and small particles increase to 48% (Fig. 6). Although
755 small particles overwhelmingly dominated particle abundance across the slope region of the SCS, their
contribution to the POC flux was notably lower than that of large particles (Fig. 10). This apparent disconnect
between numerical dominance and carbon export efficiency underscores the importance of particle size in
determining vertical carbon flux (Cram et al., 2018). Smaller particles tend to have lower sinking velocities due to
their higher surface-area-to-volume ratios and reduced mass, which makes them more susceptible to microbial
760 degradation, grazing, and disaggregation in the upper ocean (Riley et al., 2012; Durkin et al., 2015). In contrast,
large particles—such as fast-sinking marine snow aggregates, fecal pellets, and large phytoplankton or
zooplankton carcasses—settle more rapidly and are therefore more efficient vehicles for transporting organic
carbon to depth (Iversen et al., 2010; Forest et al., 2012). Previous studies have shown that large and small particles
765 differ markedly in their carbon export efficiency. Previous studies have also documented that, despite being
numerically less abundant, large particles can disproportionately contribute to the bulk of vertical carbon flux.
Steinberg et al. (2023) found that large aggregates and zooplankton fecal pellets were the primary drivers of POC
flux in the northeast subarctic Pacific, due to their rapid sinking and high carbon content. However, Similarly, Dunne
et al. (2007) highlighted that small particles are more likely to be retained and remineralized in the upper water
column, limiting their export potential in the ocean. In our study, the dominance of small particles in abundance
770 but their relatively minor role in POC flux suggests that carbon export efficiency in the SCS slope region is largely
regulated by the production and fate of large, fast-sinking particles.

The vertical partitioning of POC flux between small particles and large particles also revealed distinct depth-
dependent patterns (Supplementary Fig. S5). In the upper 200 m, small particles contributed an average of 19%

带格式的: 字体: Times New Roman

$\pm 9\%$ to the total POC flux, while large particles dominated with $81\% \pm 9\%$. Below 200 m, the relative contribution of small particles increased to $28\% \pm 12\%$, whereas that of large particles declined to $72\% \pm 12\%$. The enhanced contribution of small particles at depth was statistically significant (t-test, $p < 0.05$). Specifically, the relative contribution of small particles to total POC flux increased progressively with depth (Fig. S3a), while that of large particles showed a corresponding decline (Fig. S3b). This trend suggests that, although large particles dominate carbon export in the upper ocean, their influence diminishes with depth, whereas small particles become increasingly important in the mesopelagic zone and below. Several mechanisms may account for this shift. Large particles, such as fecal pellets and marine snow aggregates, typically sink rapidly and can reach depth with relatively little degradation (Turner, 2015). However, they are also more prone to fragmentation and microbial decomposition during descent, especially in the upper mesopelagic zone (Stamieszkin et al., 2017). As these large particles disaggregate, they contribute to the pool of smaller, slower-sinking particles, thereby increasing the relative contribution of small particles to the total flux at greater depths. In contrast, small particles—although less efficient in transporting carbon due to their slower sinking velocities and higher residence times—can persist longer in the water column. On the other hand, as discussed in Section 4.1, nepheloid layers were observed in the bottom waters along the SCS slope, particularly at stations S2 and S10. This process can introduce substantial amounts of fine sediment particles into the water column through resuspension and lateral transport (Zhou et al., 2020; Chen et al., 2024), further contributing to the increased proportion of small particles in the mesopelagic POC flux. Therefore, the elevated contribution of small particles to POC flux in the mesopelagic layer may reflect not only the progressive disaggregation of larger particles during sinking, but also the influence of resuspended fine sediments associated with nepheloid layers. Their accumulation with depth may reflect both the transformation of larger particles and the presence of suspended or laterally transported material from nepheloid layers (Zhou et al., 2020; Chen et al., 2024). These observations highlight the dynamic nature of particle flux attenuation and transformation with depth in this region.

4.4 Influence of mesoscale eddies on particle distribution and carbon flux

Mesoscale eddies are highly frequent in the SCS, with 230 eddies generated on average each year (Jin et al., 2024). These eddies exert a profound influence on regional biogeochemical processes (Xiu and Chai, 2011; Guo et al., 2015; Xu et al., 2025). Accounting for their impact is essential when examining particle characteristics and carbon export in this dynamic region. Mesoscale eddies exert a significant influence on the distribution and export of particles in the ocean, primarily through their effects on vertical nutrient fluxes, biological production, and particle transport (Shih et al., 2020; Zhang et al., 2020). In this study, two contrasting eddy regimes were encountered: an anticyclonic eddy influencing stations S4 and S5, and a cyclonic eddy encompassing the periphery of stations S11 and S12 (Fig. 1d). The comparison between cyclonic and anticyclonic eddy stations revealed distinct differences in vertical nutrients distribution, concentrations, phytoplankton biomass, particle characteristics and POC fluxes, highlighting the contrasting impacts of these two types of mesoscale eddies on carbon export processes. At the cyclonic eddy stations (S11 and S12), nutrient concentrations in the upper 5200 m, particularly between 50 and 200 m depth, nitrate and phosphate, were significantly elevated compared to those at the anticyclonic eddy stations (S4 and S5) (Supplementary Fig. S1a-c2, t-test, $p < 0.01$). Taking nitrate as an example, at the 75 m depth, the concentration at station S11 reached as high as $9.34 \mu\text{mol L}^{-1}$, whereas much lower values

带格式的: 字体: Times New Roman

带格式的: 字体: Times New Roman

were observed at stations S4 and S5, with concentrations of only 0.40 and 1.27 $\mu\text{mol L}^{-1}$, respectively. This nutrient enrichment likely resulted from upwelling processes induced by the cyclonic eddy, which supplied subsurface nutrients to the euphotic zone (Guidi et al., 2012; Zhou et al., 2021). Several studies have documented similar processes in the SCS, where cyclonic eddies promote the upward transport of nutrients from the subsurface, while anticyclonic eddies have the opposite effect, deepening the nutricline and resulting in nutrient depletion in the upper water column (Shih et al., 2020; Xu et al., 2025). Consequently, phytoplankton biomass, reflected by Chl *a* concentrations, responded to these changes in vertical nutrient distribution. Notably, Chl *a* concentrations in the upper water column, were substantially higher at station S11 and S12 compared to S4 and S5 (Supplementary Fig. S1d). The integrated Chl *a* concentrations above 75 m were 14.34 and 19.18 mg m^{-2} at S11 and S12, respectively, exceeding the values observed at S4 (13.95 mg m^{-2}) and S5 (9.19 mg m^{-2}). These results suggest that under influence of the cyclonic eddy, phytoplankton production in the upper water column at S11 and S12 was enhanced relative to the anticyclonic eddy-affected stations S4 and S5. Accordingly, PVC at stations S11 and S12 was significantly higher than that at stations S4 and S5 throughout most of the water column from the surface to 800 m (Fig. 6a). The two regions also exhibited distinct patterns in the size composition of PVC (Fig. 6b-c). At stations S4 and S5, small particles generally accounted for more than 40% of the total PVC throughout the water column, with average contributions of $45\% \pm 6\%$ (mean \pm SD) and $55\% \pm 10\%$ (mean \pm SD), respectively. In contrast, the proportion of small particles at stations S11 and S12 was noticeably lower, averaging $35\% \pm 8\%$ (mean \pm SD) and $30\% \pm 7\%$ (mean \pm SD), respectively, and typically remaining below 40%. This contrast indicates that the two types of mesoscale eddies exert different influences on the particle size composition. Although this study did not include direct analysis of phytoplankton community composition, previous studies have shown that cyclonic eddies could promote the growth and proliferation of large-sized phytoplankton, such as diatoms, allowing them to become dominant within the community (Shih et al., 2020; Chenillat et al., 2024). These larger phytoplankton are more prone to form aggregates through intercellular coagulation (Panaïotis et al., 2024), thereby contributing to the generation of larger particles. Moreover, they provide a favorable food source for large zooplankton, which were indeed observed in greater abundance at stations S11 and S12 in this study (Supplementary Fig. 2c). Together, these mechanisms likely contributed to the higher proportion of large particles in the total PVC at stations S11 and S12. In contrast, anticyclonic eddies, characterized by nutrient depletion, tend to favor the proliferation of smaller phytoplankton groups, such as picophytoplankton (Dai et al., 2020; Zhang et al., 2023). Compared to diatoms and other large phytoplankton groups, picophytoplankton are less likely to form aggregates through cell coagulation (Guidi et al., 2009). Instead, they are more readily consumed by small zooplankton such as ciliates, channeling biomass into the microbial loop rather than into fast-sinking particles (Honjo et al., 2008). The abundance of large zooplankton at stations S4 and S5 was also relatively low (Supplementary Fig. S2a, b). These conditions weaken the formation of large particles here, thereby contributing to the increased proportion of small particles observed at stations S4 and S5 compared to that in S11 and S12. Therefore, cyclonic and anticyclonic eddies in the SCS exert different influences on particle concentration and size composition by altering nutrient availability and phytoplankton production processes. Cyclonic eddies tend to promote the formation of large particles, while anticyclonic eddies are associated with an increased proportion of small particles, was also higher in the cyclonic eddy region (Fig. S2d). Enhanced primary production stimulated by nutrient availability led to greater production of organic particles. In response to elevated phytoplankton biomass, particle abundance and PVC were substantially higher at the cyclonic eddy stations (Fig. S3, *t*-test, $p < 0.01$). This increase in particulate material

带格式的: 字体: Times New Roman

855 contributed to the elevated POC fluxes observed at S11 and S12 across all depths. Notably, POC fluxes at these stations exceeded $100 \text{ mg C m}^{-2} \text{ d}^{-1}$ in the upper layers and remained relatively high at deeper depths (Fig. 9), suggesting efficient vertical transport of organic carbon facilitated by particle aggregation and rapid sinking. In contrast, anticyclonic eddies are typically associated with downwelling and thermocline deepening, leading to nutrient limitation and reduced surface productivity (Stramma et al., 2013). This pattern is evident in the nutrient and Chl *a* distributions observed at stations S4 and S5 in this study (Supplementary Fig. S2). The low productivity in this region likely contributed to the reduced particle concentrations and diminished carbon fluxes (Supplementary Fig. S3). Overall, cyclonic eddies enhanced carbon export by promoting nutrient injection, stimulating primary production, and facilitating the formation and vertical transfer of sinking particles. In contrast, anticyclonic eddies suppressed these processes, leading to lower particle abundance and weaker POC fluxes. These findings emphasize the pivotal role of mesoscale physical dynamics in regulating biological pump efficiency and carbon sequestration in oligotrophic ocean regions.

865 How do changes in particle concentration and size composition between cyclonic and anticyclonic eddy regions affect POC export flux? Flux estimates derived from UVP data provide a valuable means to explore this question. In this study, we applied the method proposed by Guidi et al. (2008a), which estimates POC flux from UVP-derived particle size spectra using an empirical relationship originally developed from a global sediment trap dataset. This method has since been widely applied across various oceanic regions for consistency and comparability (Ramondenc et al., 2016; Clements et al., 2023; Wang et al., 2004a). We acknowledge that regional differences may influence the absolute values of the estimated fluxes, the method remains robust for evaluating relative differences among stations within this study. In terms of carbon flux, the POC export at the cyclonic eddy influenced stations (S11 and S12) was significantly higher than that at the anticyclonic eddy influenced stations (S4 and S5) (Fig. 8a, *t*-test, $p < 0.01$). This difference was pronounced in the upper water column. For example, at 50 m depth, the POC flux at station S11 reached as high as $122 \text{ mg C m}^{-2} \text{ d}^{-1}$, while values at stations S4 and S5 were only 37 and $52 \text{ mg C m}^{-2} \text{ d}^{-1}$, respectively (Fig. 8a). A similar pattern was observed in the mesopelagic layer below 200 m, where fluxes at S11 and S12 remained markedly higher than those at S4 and S5. Quantitatively, the POC flux in the cyclonic eddy region was more than twice that in the anticyclonic eddy region. Several studies have demonstrated that cyclonic eddies can enhance POC export by stimulating primary productivity in the upper water column in the SCS, whereas anticyclonic eddies tend to suppress it (Li et al., 2017; Zhang et al., 2020; Zhou et al., 2020). The significant correlation observed in this study between POC flux and Chl *a* (Fig. 9) further supports this relationship, indicating that increased phytoplankton biomass due to mesoscale processes is conducive to higher carbon export. An additional insight is that the contribution of small particles to the POC flux was higher in the anticyclonic eddy influenced region compared to the cyclonic eddy influenced region, whereas the opposite pattern was observed for large particles (Fig. 8b, c). This pattern highlights the distinct export pathways associated with different eddy regimes. In anticyclonic eddies, although small particles still contribute less to the POC flux than large particles, their relative contribution is noticeably higher compared to that in cyclonic eddies. In contrast, cyclonic eddies enhance the formation of large, fast-sinking particles (Fig. 6), leading to a reduced proportional contribution of small particles to vertical carbon export. These findings provide important implications for carbon export modeling. Most biogeochemical models assume a uniform particle sinking behavior or rely on bulk POC estimates, potentially underestimating the variability introduced by mesoscale physical processes (Bisson et al., 2018; Nowicki et al., 2022). Our findings emphasize the need for incorporating size-resolved particle fluxes and eddy-specific dynamics into carbon export models, particularly in regions where eddy activity is intense and

895 persistent. Accounting for the contributions of particles with different size under varying eddy regimes will
improve model accuracy in representing depth-dependent carbon attenuation and export efficiency.

900 In the SCS, previous studies have highlighted the critical role of mesoscale eddies in regulating
biogeochemical processes. For example, Li et al. (2017) found that the POC flux in cyclonic eddies was 41%
higher than that during the non-cyclonic eddy period in the central SCS. Liu et al. (2020) studied zooplankton
community structure in the northern SCS and found that decreased zooplankton biomass, abundances, and
905 biovolumes were observed in the anticyclonic eddy compared to the edge and outside of the anticyclonic eddy.
Shih et al. (2020) investigated the effect of eddies (cold and warm eddies) on the nutrient supply to the euphotic
zone and the organic carbon export in the northern SCS, and found that the POC flux associated with the cold
eddies was significantly higher than that associated with the warm eddy. This study, based on high-resolution
observations of particle distribution and associated POC fluxes, reveals the contrasting effects of cyclonic and
910 anticyclonic eddies on particle production and carbon export. Cyclonic eddies in the SCS can act as biological
pump enhancers, particularly along the slope regions where topography and eddy interactions are complex. In
contrast, anticyclonic eddies, by suppressing the upward transport of nutrients, can lead to reduced biological
production and consequently lower carbon export.

910 4.5 Data uncertainties

The high-resolution UVP observations allowed us to capture fine-scale vertical and spatial variability in
particle abundance, PVC, and POC fluxes, which have been difficult to resolve using conventional sampling
techniques. While this study provides valuable data and information, its limitations should also be acknowledged.
The estimation of particle size and abundance was based on data from the UPV, which, despite its utility for *in situ*
915 imaging, has limited sensitivity to particles smaller than $\sim 100 \mu\text{m}$ and may underestimate the contribution of very
fine particles to the total POC flux (Picheral et al., 2010). The conversion of particle volume to carbon flux relies
on empirical relationships that may not fully capture spatial and temporal variability in particle composition and
carbon content in the study area (Guidi et al., 2008a; Fender et al., 2019). Future studies incorporating direct flux
measurements (e.g., sediment traps or thorium-based methods) would help reduce uncertainties and improve the
920 quantification of particle-mediated carbon export.

5 Conclusion

Using high-resolution *in situ* observations from the UPV, this study provides a detailed characterization of
particle distributions and particle-mediated carbon fluxes along the continental slope of the SCS. The results
925 demonstrate distinct spatial and vertical patterns in particle distribution and size composition along the SCS slope,
and elucidate the mechanisms by which mesoscale eddy processes influence particle characteristics and associated
carbon export fluxes. Both particle abundance and volume concentration were elevated at the inner slope stations
and in the cyclonic eddy-influenced region, while lower values were observed in other regions. In terms of size
composition, small particles ($\text{ESD} < 500 \mu\text{m}$) overwhelmingly dominated in numerical abundance throughout
930 the water column, whereas large particles ($\text{ESD} \geq 500 \mu\text{m}$) contributed disproportionately to the particle volume
concentration and POC flux. Although small particles numerically dominate, their relatively lower volume and
slower sinking rates limit their contribution to vertical POC export compared to large particles. In terms of
mesoscale eddy influence, our observations revealed pronounced differences in particle characteristics and carbon

带格式的: 字体: Times New Roman

带格式的: 字体: Times New Roman

935 export between cyclonic and anticyclonic eddies. Cyclonic eddies were associated with elevated particle
concentrations, a reduced proportion of small particles, and an increased contribution of large particles. In contrast,
940 anticyclonic eddies showed a higher proportion of small particles and a reduced share of large particles. These
differences are primarily driven by eddy-induced changes in upper-layer nutrient availability and phytoplankton
production. Consequently, the POC flux in cyclonic eddy-influenced regions was consistently higher than in
945 anticyclonic regions throughout the water column. abundance and POC flux, shaped by hydrographic structure,
biological production, and mesoscale physical processes. Small particles (ESD < 500 μm) overwhelmingly
dominated in numerical abundance throughout the water column, but large particles (ESD \geq μm) contributed
disproportionately to vertical carbon export due to their higher sinking velocities. Mesoscale eddies were found to
significantly modulate particle dynamics and export efficiency. Stations located at the edge of a cyclonic eddy
exhibited elevated particle concentrations and POC fluxes, whereas those within an anticyclonic eddy displayed
markedly reduced values. These contrasting signatures reflect the differential impacts of mesoscale physical
processes on nutrient availability and particle production. The contribution of small particles to POC flux increased
with depth, suggesting that disaggregation processes and lateral transport mechanisms, such as nepheloid layer
formation, play a role in deep particle dynamics.

950 This study represents one of the first efforts to apply size-resolved UVP observations to characterize depth-
dependent particle fluxes in the SCS. By resolving the relative roles of small and large particles and linking their
export patterns to mesoscale forcing, our results provide new insights into the size-selective processes governing
vertical carbon transport in marginal seas. These findings highlight the value of combining optical imaging tools
with hydrographic context to constrain particle-mediated carbon export, which offers process-level evidence that
can inform the representation of size-structured export fluxes in global biogeochemical models.

955 **Data Availability Statement**

Data available on request from the authors.

Author Contribution

960 SG: Conceptualization, Data curation, Formal analysis, Methodology, Software, Visualization, Writing-original
draft preparation. MZ: Data curation, Formal analysis, Investigation, Methodology, Validation. WX: Data curation,
Methodology. SZ: Investigation. SL: Data curation, Investigation. YW: Data curation, Investigation. JD: Data
curation. CZ: Visualization. XS: Conceptualization, Data curation, Funding acquisition, Project administration,
Supervision, Writing-review&editing.

Competing interests

The authors declare that they have no conflict of interest.

965 **Disclaimer**

Publisher's note: Copernicus Publications remains neutral with regard to jurisdictional claims made in the text,
published maps, institutional affiliations, or any other geographical representation in this paper. While
Copernicus Publications makes every effort to include appropriate place names, the final responsibility lies with
the authors.

970 **Acknowledgements**

We thank the crew and captain of the R/V *Nanfeng* for the logistic support during the cruise. This work was supported by the National Key Research and Development Program of China (No. 2024YFE0114300), the National Natural Science Foundation of China (No. 32371619, U2006206), the National Basic Research Program of China (No. 2014CB441504), the International Partnership Program of Chinese Academy of Sciences (No. 133137KYSB20200002, 121311KYSB20190029).

Financial support

This research has been supported by the National Key Research and Development Program of China (No. 2024YFE0114300), the National Natural Science Foundation of China (No. 32371619, U2006206), the National Basic Research Program of China (No. 2014CB441504), the International Partnership Program of Chinese Academy of Sciences (No. 133137KYSB20200002, 121311KYSB20190029).

References

Accardo, A., Laxenaire, R., Baudena A., Speich, S., Kiko, R., Stemman, L.: Intense and localized export of selected marine snow types at eddy edges in the South Atlantic Ocean, *Biogeosciences*, 22, 1183–1201, <https://doi.org/10.5194/bg-22-1183-2025>, 2025.

985 [Bandara, K., Varpe, Ø., Wijewardene, L., Tverberg, V., Eiane, K.: Two hundred years of zooplankton vertical migration research. *Biol. Rev.*, 96, 1547–1589, <https://doi.org/10.1111/brv.12715>, 2021.](#)

[Barlow, R., Lamont, T., Morris, T., Sessions, H., van den Berg, M.: Adaptation of phytoplankton communities to mesoscale eddies in the Mozambique Channel. *Deep-Sea Res. PT II*, 100, 106–118, <https://doi.org/10.1016/j.dsr2.2013.10.020>, 2014.](#)

990 [Barone, B., Church, M. J., Dugenne, M., Hawco, N. J., Jahn, O., White, A. E., John, S. G., Follows, M. J., DeLong, E. F., Karl, D. M.: Biogeochemical dynamics in adjacent mesoscale eddies of opposite polarity. *Global Biogeochem. Cy.*, 36\(2\), e2021GB007115, <https://doi.org/10.1029/2021GB007115>, 2022.](#)

[Bisson, K. M., Siegel, D. A., DeVries, T., Cael, B. B., Buesseler, K. O.: How data set characteristics influence ocean carbon export models. *Global Biogeochem. Cy.*, 32\(9\), 1312–1328, <https://doi.org/10.1029/2018GB005934>, 2018.](#)

995 [Boss, E., Guidi, L., Richardson, M. J., Stemmann, L., Gardner, W., Bishop, J. K., Anderson, R. F., Sherrell, R. M.: Optical techniques for remote and in-situ characterization of particles pertinent to GEOTRACES. *Prog. Oceanogr.*, 133, 43–54, <https://doi.org/10.1016/j.pocan.2014.09.007>, 2015.](#)

1000 [Boyd, P. W., Claustre, H., Levy, M., Siegel, D. A., Weber, T.: Multi-faceted particle pumps driven carbon sequestration in the ocean. *Nature*, 568\(7752\), 327–335, <https://doi.org/10.1038/s41586-019-1098-2>, 2019.](#)

[Buesseler, K. O., Antia, A., Chen, M., Fowler, S. W., Gardner, W. D., Gustafsson, O., Harada, K., Michaels, A. F., van der Loeff, M. R., Sarin, M., Steinberg, D. K., Trull, T.: An assessment of the use of sediment traps for estimating upper ocean particle fluxes. *J. Mar. Res.*, 65, 345–416, <https://doi.org/10.1357/002224007781567621>, 2007.](#)

1005 [Buongiorno Nardelli, B., Droghei, R., Santoleri, R.: Multi-dimensional interpolation of SMOS sea surface](#)

带格式的: 字体: (默认) Times New Roman

带格式的: 字体: 五号

带格式的: 字体: (默认) Times New Roman

域代码已更改

带格式的: 字体: (默认) Times New Roman, 10 磅, 非加粗, 字体颜色: 蓝色, 图案: 清除

带格式的: 字体: (默认) Times New Roman

salinity with surface temperature and in situ salinity data. *Remote Sens. Environ.*, 180, 392–402, <http://dx.doi.org/10.1016/j.rse.2015.12.052>, 2016.

1010 Cai, P., Zhao, D., Wang, L., Huang, B., Dai, M.: Role of particle stock and phytoplankton community structure in regulating particulate organic carbon export in a large marginal sea. *J. Geophys. Res.*, 120, 2063–2095, <https://doi.org/10.1002/2014JC010432>, 2015.

Chen, T., Liu, X. L., Bian, C. W., Zhang, S. T., Ji, C. S., Wu, Z. S., Jia, Y. G.: Nepheloid layer structure and variability along the highly energetic continental margin of the northern South China Sea. *J. Geophys. Res.*, 129(2), e2023JC020072, <https://doi.org/10.1029/2023JC020072>, 2024.

1015 Chenillat, F., Deshaies, E., Arens, A., Penven, P.: Role of mesoscale eddies in the biogeochemistry of the Mozambique Channel. *Front. Mar. Sci.*, 11, 1402776, doi: 10.3389/fmars.2024.1402776, 2024.

Clements, D. J., Yang, S., Weber, T., McDonnell, A. M. P., Kiko, R., Stemmann, L., Bianchi, D.: New estimate of organic carbon export from optical measurements reveals the role of particle size distribution and export horizon. *Global Biogeochem. Cy.*, 37, e2022GB007633, <https://doi.org/10.1029/2022GB007633>, 2023.

1020 Cram, J. A., Weber, T., Leung, S. W., McDonnell, A. M., Liang, J. H., Deutsch, C.: The role of particle size, ballast, temperature, and oxygen in the sinking flux to the deep sea. *Global Biogeochem. Cy.*, 32(5), 858–876, <https://doi.org/10.1029/2017GB005710>, 2018.

Cram, J. A., Fuchsman, C. A., Duffy, M. E., Pretty, J. L., Lekanoff, R. M., Neibauer, J. A., Leung, S. W., Huebert, K. B., Weber, T. S., Bianchi, D., Evans, N., Devol, A. H., Keil, R. G., McDonnell, A. M. P.: Slow particle remineralization, rather than suppressed disaggregation, drives efficient flux transfer through the eastern tropical North Pacific oxygen deficient zone. *Global Biogeochem. Cy.*, 36, e2021GB007080, <https://doi.org/10.1029/2021GB007080>, 2022.

1025 Dai, S., Zhao, Y. F., Liu, H. J., Hu, Z. Y., Zheng, S., Zhu, M. L., Guo, S. J., Sun, X. X.: The effects of a warm-core eddy on chlorophyll *a* distribution and phytoplankton community structure in the northern South China Sea in spring 2017. *J. Marine Syst.*, 210, 103396, <https://doi.org/10.1016/j.jmarsys.2020.103396>, 2020.

1030 Dunne, J. P., Sarmiento, J. L., Gnanadesikan, A.: A synthesis of global particle export from the surface ocean and cycling through the ocean interior and on the seafloor. *Global Biogeochem. Cy.*, 21(4), GB4006, <https://doi.org/10.1029/2006GB002907>, 2007.

Durkin, C. A., Estapa, M. L., Buesseler, K. O.: Observations of carbon export by small sinking particles in the upper mesopelagic. *Mar. Chem.*, 175, 72–81, <https://doi.org/10.1016/j.marchem.2015.02.011>, 2015.

1035 Fender, C. K., Kelly, T. B., Guidi, L., Ohman, M. D., Smith M, C., Stukel, M. R.: Investigating particle size-flux relationships and the biological pump across a range of plankton ecosystem states from coastal to oligotrophic. *Front. Mar. Sci.*, 6, 603, <https://doi.org/10.3389/fmars.2019.00603>, 2019.

Forest, A., Stemmann, L., Picheral, M., Burdorf, L., Robert, D., Fortier, L., Babin, M.: Size distribution of particles and zooplankton across the shelf-basin system in southeast Beaufort Sea: combined results from an Underwater Vision Profiler and vertical net tows. *Biogeosciences*, 9, 1301–1320, <https://doi.org/10.5194/bg-9-1301-2012>, 2012.

1040 González-Estrada, E., Cosmes, W.: Shapiro – Wilk test for skew normal distributions based on data transformations. *J. Stat. Comput. Sim.*, 89, 3258–3272, <https://doi.org/10.1080/00949655.2019.1658763>, 2019.

1045 Gorsky, G., Picheral, M., Stemmann, L.: Use of the Underwater Video Profiler for the study of aggregate dynamics in the North Mediterranean. *Estuar. Coast. Shelf S.*, 50, 121–128,

带格式的: 字体: (默认) Times New Roman, 10 磅, 字体颜色: 自动设置, 图案: 清除

带格式的: 字体: Times New Roman

带格式的: 字体: Times New Roman

- <https://doi.org/10.1006/ecss.1999.0539>, 2000.
- Guidi, L., Stemann, L., Legendre, L., Picheral, M., Prieur, L., Gorsky, G.: Vertical distribution of aggregates (>100 μm) and mesoscale activity in the Northeastern Atlantic: effects on the deep vertical export of surface carbon. *Limnol. Oceanogr.*, 52, 7–18, <https://doi.org/10.4319/lo.2007.52.1.0007>, 2007.
- 1050 Guidi, L., Jackson, G. A., Stemann, L., Miquel, J. C., Picheral, M., Gorsky, G.: Relationship between particle size distribution and flux in the mesopelagic zone. *Deep-Sea Res. PT I*, 55, 1364–1374, <https://doi.org/10.1016/j.dsr.2008.05.014>, 2008a.
- Guidi, L., Gorsky, G., Claustre, H., Miquel, J. C., Picheral, M., Stemann, L.: Distribution and fluxes of aggregates >100 μm in the upper kilometer of the South-Eastern Pacific. *Biogeosciences*, 5, 1361–1372, <https://doi.org/10.5194/bg-5-1361-2008>, 2008b.
- 1055 Guidi, L., Stemann, L., Jackson, G. A., Ibanez, F., Claustre, H., Legendre, L., Picheral, M., Gorsky, G.: Effects of phytoplankton community on production, size, and export of large aggregates: a world-ocean analysis. *Limnol. Oceanogr.*, 54(6), 1951–1963, <https://doi.org/10.4319/lo.2009.54.6.1951>, 2009.
- Guidi, L., Calil, P. H. R., Duhamel, S., Björkman, K. M., Doney, S. C., Jackson, G. A., Li, B. L., Church, M. J., Tozzi, S., Kolber, Z. S., Richards, K. J., Fong, A. A., Letelier, R. M., Gorsky, G., Stemann, L., Karl, D. M.: Does eddy-eddy interaction control surface phytoplankton distribution and carbon export in the North Pacific Subtropical Gyre? *J. Geophys. Res.*, 117, G02024, <https://doi.org/10.1029/2012JG001984>, 2012.
- 1060 Guidi, L., Legendre, L., Reygondeau, G., Uitz, J., Stemann, L., Henson, S. A.: A new look at ocean carbon remineralization for estimating deepwater sequestration. *Global Biogeochem. Cy.*, 29(7), 1044–1059, <https://doi.org/10.1002/2014GB005063>, 2015.
- 1065 Guidi, L., Chaffron, S., Bittner, L., Eveillard, D., Larhlmi, A., Roux, S., Darzi, Y., Audic, S., Berline, L., Brum, J. R., Coelho, L. P., Espinoza, J. C. I., Malviya, S., Sunagawa, S., Dimier, C., Kandels-Lewis, S., Picheral, M., Poulain, J., Searson, S., Consortium Coordinators, T. O., Stemann, L., Not, F., Hingamp, P., Speich, S., Follows, M., Karp-Boss, L., Boss, E., Ogata, H., Pesant, S., Weissenbach, J., Wincker, P., Acinas, S. G., Bork, P., de Vargas, C., Iudicone, D., Sullivan, M. B., Raes, J., Karsenti, E., Bowler, C., Gorsky, G.: Plankton networks driving carbon export in the oligotrophic ocean. *Nature*, 532, 465–470, <https://doi.org/10.1038/nature16942>, 2016.
- [Guo, M. X., Chai, F., Xiu, P., Li, S. Y., Rao, S.: Impacts of mesoscale eddies in the South China Sea on biogeochemical cycles. *Ocean Dynam.*, 65, 1335–1352, <https://doi.org/10.1007/s10236-015-0867-1>, 2015.](https://doi.org/10.1007/s10236-015-0867-1)
- 1075 Hong, Q. Q., Peng, S. Y., Zhao, D. C., Cai, P. H.: Cross-shelf export of particulate organic carbon in the northern South China Sea: Insights from a ²³⁴Th mass balance. *Prog. Oceanogr.*, 193, 102532, <https://doi.org/10.1016/j.pocean.2021.102532>, 2021.
- [Honjo, S., Manganini, S. J., Krishfield, R. A., Francois, R.: Particulate organic carbon fluxes to the ocean interior and factors controlling the biological pump: A synthesis of global sediment trap programs since 1983. *Prog. Oceanogr.*, 76, 217–285, <https://doi.org/10.1016/j.pocean.2007.11.003>, 2008.](https://doi.org/10.1016/j.pocean.2007.11.003)
- 1080 [Harms, N. C., Lahajnar, N., Gaye, B., Rixen, T., Schwarz-Schampera, U., Emeis, K.: Sediment trap-derived particulate matter fluxes in the oligotrophic subtropical gyre of the South Indian Ocean. *Deep-Sea Res. PT I*, 183, 104924, <https://doi.org/10.1016/j.dsr.2020.104924>, 2021.](https://doi.org/10.1016/j.dsr.2020.104924)
- Iversen, M. H., Nowald, N., Ploug, H., Jackson, G. A., Fischer, G.: High resolution profiles of vertical particulate organic matter export off Cape Blanc, Mauritania: degradation processes and ballasting effects. *Deep-Sea Res.*
- 1085

带格式的: 字体: (默认) Times New Roman

域代码已更改

带格式的: 超链接, 字体: (默认) Times New Roman, 10 磅, 字体颜色: 自动设置, 图案: 清除

带格式的: 字体: (默认) Times New Roman, 10 磅

带格式的: 字体: 10 磅

带格式的: 字体: (默认) Times New Roman, 10 磅

带格式的: 字体: 10 磅

- PT I, 57(6), 771–784, <https://doi.org/10.1016/j.dsr.2010.03.007>, 2010.
- James, R.: Applications of the Underwater Vision Profiler for particle annotation in the oligotrophic North Pacific subtropical gyre, M.S. thesis, University of Hawai at Manoa, USA, 63 pp., 2024.
- Jia, Y. G., Tian, Z. C., Shi, X. F., Liu, J. P., Chen, J. X., Liu, X. L., Ye, R. J., Ren, Z. Y., Tian, J. W.: Deep-sea sediment resuspension by internal solitary waves in the northern South China Sea. *Sci. Rep.*, 9, 12137, <https://doi.org/10.1038/s41598-019-47886-y>, 2019.
- 1090 <https://doi.org/10.1038/s41598-019-47886-y>, 2019.
- [Jin, Y., Jin, M., Wang, D., Dong, C.: Statistical analysis of multi-year South China Sea eddies and exploration of eddy classification. *Remote Sens.*, 16, 1818. <https://doi.org/10.3390/rs16101818>, 2024.](https://doi.org/10.3390/rs16101818)
- Jouandet, M. P., Trull, T. W., Guidi, L., Picheral, M., Ebersbach, F., Stemmann, L., Blain, S.: Optical imaging of mesopelagic particles indicates deep carbon flux beneath a natural iron-fertilized bloom in the Southern Ocean. *Limnol. Oceanogr.*, 56(3), 1130–1140, <https://doi.org/10.4319/lo.2011.56.3.1130>, 2011.
- 1095 Jouandet, M. P., Jackson, G. A., Carlotti, F., Picheral, M., Stemmann, L., Blain, S.: Rapid formation of large aggregates during the spring bloom of Kerguelen Island: observations and model comparisons. *Biogeosciences*, 11, 4393–4406, <https://doi.org/10.5194/bg-11-4393-2014>, 2014, 2014.
- 1100 Kahru, M., Mitchell, B. G., Gille, S. T., Hewes, C. D., Holm-Hansen, O.: Eddies enhance biological production in the Weddell-Scotia Confluence of the Southern Ocean. *Geophys. Res. Lett.*, 34, L14603, <https://doi.org/10.1029/2007GL030430>, 2007.
- Kiko, R., Biastoch, A., Brandt, P., Cravatte, S., Hauss, H., Hummels, R., Kriest, I., Marin, F., MaDonnell, A. M. P., Oschlies, A., Picheral, M., Schwarzkopf, F. U., Thurnherr, A. M., Stemmann, L.: Biological and physical influences on marine snowfall at the equator. *Nat. Geosci.*, 10(11), 852–858, <https://doi.org/10.1038/ngeo3042>, 2017.
- 1105 Kiko, R., Picheral, M., Antoine, D., Babin, M., Berline, L., Biard, T., Boss, E., Brandt, P., Carlotti, F., Christiansen, S., Coppola, L., de la Cruz, L., Diamond-Riquier, E., de Madron, X. D., Elineau, A., Gorsky, G., Guidi, L., Hauss, H., Irissou, J. O., Karp-Boss, L., Karstensen, J., Kim, D., Lekanoff, R. M., Lombard, F., Lopes, R. M., Marec, C., McDonnell, A. M. P., Niemeyer, D., Noyon, M., O'Daly, S. H., Ohman, M. D., Pretty, J. L., Rogge, A., Searson, S., Shibata, M., Tanaka, Y., Tanhua, T., Taucher, J., Trudnowska, E., Turner, J. S., Waite, A., Stemmann, L.: A global marine particle size distribution dataset obtained with the Underwater Vision Profiler 5. *Earth Syst. Sci. Data*, 14, 4315–4337, <https://doi.org/10.5194/essd-14-4315-2022>, 2022.
- 1115 Kriest, I.: Different parameterizations of marine snow in a 1D-model and their influence on representation of marine snow, nitrogen budget and sedimentation. *Deep-Sea Res. PT I*, 49(12), 2133–2162, [https://doi.org/10.1016/S0967-0637\(02\)00127-9](https://doi.org/10.1016/S0967-0637(02)00127-9), 2002.
- Kwon, E. Y., Primeau, F., Sarmiento, J. L.: The impact of remineralization depth on the air-sea carbon balance. *Nat. Geosci.*, 2(9), 630–635, <https://doi.org/10.1038/ngeo612>, 2009.
- 1120 Li, H. L., Wiesner, M. G., Chen, J. F., Ling, Z., Zhang, J. J., Ran, L. H.: Long-term variation of mesopelagic biogenic flux in the central South China Sea: Impact of monsoonal seasonality and mesoscale eddy. *Deep-Sea Res. PT I*, 126, 62–72, <https://doi.org/10.1016/j.dsr.2017.05.012>, 2017.
- Liu, H. J., Zhu, M. L., Guo, S. J., Zhao, X. H., Sun, X. X.: Effects of an anticyclonic eddy on the distribution and community structure of zooplankton in the South China Sea northern slope. *J. Marine Syst.*, 205, 103311, <https://doi.org/10.1016/j.jmarsys.2020.103311>, 2020.
- 1125 Liu, J. A., Du, J. Z., Wu, Y., Liu, S. M.: Radium-derived water mixing and associated nutrient in the northern South China Sea. *Front. Mar. Sci.*, 9, 874547, <https://doi.org/10.3389/fmars.2022.874547>, 2022.

- Liu, Z. F., Zhao, Y. L., Colin, C., Statteger, K., Wiesner, M. G., Huh, C. A., Zhang, Y. W., Li, X. J., Sompongchaiyakul, P., You, C. F., Huang, C. Y., Liu, J. T., Siringan, F. P., Le, K. P., Sathiamurthy, E., Hantoro, W. S., Liu, J. G., Tuo, S. T., Zhao, S. H., Zhou, S. W., He, Z. D., Wang, Y. C., Bunsomboonsakul, S., Li, Y.: Source-to-sink transport processes of fluvial sediments in the South China Sea. *Earth-Sci. Rev.*, 153, 238–273, <https://doi.org/10.1016/j.earscirev.2015.08.005>, 2016.
- Ma, Y. F., Zhou, K. B., Chen, W. F., Chen, J. H., Yang, J. T., Dai, M. H.: Partitioning of carbon export in the euphotic zone of the oligotrophic South China Sea. *Biogeosciences*, 20, 2013–2030, <https://doi.org/10.5194/bg-20-2013-2023>, 2023.
- 1130 Maiti, K., Benitez-Nelson, C. R., Rii, Y., Bidigare, R.: The influence of a mature cyclonic eddy on particle export in the lee of Hawaii. *Deep-Sea Res. PT II*, 55(10-13), 1445–1460, <https://doi.org/10.1016/j.dsr2.2008.02.008>, 2008.
- [Mangolte, I., Lévy, M., Dutkiewicz, S., Clayton, S. Jahn, O.: Plankton community response to fronts: winners and losers. *J. Plankton Res.*: 44\(2\), 241–258, <https://doi.org/10.1093/plankt/fbac010>, 2022.](#)
- 1140 [McGillicuddy Jr., D. J.: Mechanisms of physical-biological-biogeochemical interaction at the oceanic mesoscale. *Annu. Rev. Mar. Sci.*, 8, 125–159, <https://doi.org/10.1146/annurev-marine-010814-015606>, 2016.](#)
- [Nowicki, M., DeVries, T., Siegel, D. A.: Quantifying the carbon export and sequestration pathways of the ocean's biological carbon pump. *Global Biogeochem. Cy.*, 36\(3\), e2021GB007083, <https://doi.org/10.1029/2021GB007083>, 2022.](#)
- 1145 [Oliveira, A., Vitorino, J., Rodrigues, A., Jouanneau, J. M., Dias, J. A., Weber, O.: Nepheloid layer dynamics in the northern Portuguese shelf. *Prog. Oceanogr.*, 52\(204\), 195–213, \[https://doi.org/10.1016/S0079-6611\\(02\\)00006-X\]\(https://doi.org/10.1016/S0079-6611\(02\)00006-X\), 2002.](#)
- Panaotiotis, T., Poteau, A., Riquier, É. D., Catalano, C., Courchet, L., Motreuil, S., Coppola, L., Picheral, M., Irisson, J. O.: Temporal evolution of plankton and particles distribution across a mesoscale front during the spring bloom. *Limnol. Oceanogr.*, 9999, 1–15, <https://doi.org/10.1002/lno.12566>, 2024.
- 1150 [Peterson, T. D., Whitney, F. A., Harrison, P. J.: Macronutrient dynamics in an anticyclonic mesoscale eddy in the Gulf of Alaska. *Deep-Sea Res. PT II*, 52\(7-8\), 909–932, <https://doi.org/10.1016/j.dsr2.2005.02.004>, 2005.](#)
- Picheral, M., Guidi, L., Stemmann, L., Karl, D. M., Iddaoud, G., Gorsky, G.: The Underwater Vision Profiler 5: an advanced instrument for high spatial resolution studies of particle size spectra and zooplankton. *Limnol. Oceanogr-Meth.*, 8, 462–473, <https://doi.org/10.4319/lom.2010.8.462>, 2010.
- 1155 [Picheral, M., Colin, S., Irrison, J. O.: EcoTaxa, a tool for the taxonomic classification of images: available at: <http://ecotaxa.obs-vlfr.fr><http://ecopart.obs-vlfr.fr>, 2017.](#)
- Picheral, M., Catalano, C., Brousseau, D., Claustre, H., Coppola, L., Leymarie, E., Coindat, J., Dias, F., Fevre, S., Guidi, L., Irisson, J. O., Legendre, L., Lombard, F., Mortier, L., Penkerch, C., Rogge, A., Schmechtig, C., Thibault, S., Tixier, T., Waite, A., Stemmann, L.: The Underwater Vision Profiler 6: an imaging sensor of particle size spectra and plankton, for autonomous and cabled platforms. *Limnol. Oceanogr-Meth.*, 20(2), 115–129, <https://doi.org/10.1002/lom3.10475>, 2022.
- 1160 Pretty, J. L.: Particles in the Pacific: how productivity and zooplankton relate to particles in the deep sea. M.S., thesis, University of Alaska Fairbanks, USA, 41 pp., 2019.
- 1165 Ramondenc, S., Madeleine, G., Lombard, F., Santinelli, C., Stemmann, L., Gorsky, G., Guidi, L.: An initial carbon export assessment in the Mediterranean Sea based on drifting sediment traps and the underwater vision

带格式的: 字体: Times New Roman

带格式的: 字体: (默认) Times New Roman, 10 磅

profiler data sets. Deep-Sea Res. PT I, 117, 107–119, <https://doi.org/10.1016/j.dsr.2016.08.015>, 2016.

Riley, J. S., Sanders, R., Marsay, C., Le Moigne, F. A. C., Achterberg, E. P., Poulton, A. J.: The relative contribution of fast and slow sinking particles to ocean carbon export. Global Biogeochem. Cy., 26(1), <https://doi.org/10.1029/2011GB004085>, 2012.

1170 <https://doi.org/10.1029/2011GB004085>, 2012.

[Sammartino, M., Aronica, S., Santoleri, R., Nardelli, B. B.: Retrieving Mediterranean Sea surface salinity distribution and interannual trends from multi-sensor satellite and in situ data. Remote Sens., 14, 2502. https://doi.org/10.3390/rs14102502, 2022.](https://doi.org/10.3390/rs14102502)

Shih, Y. Y., Hung, C. C., Tuo, S. H., Shao, H. J., Chow, C. H., Muller, F. L. L., Cai, Y. H.: The impact of eddies on nutrient supply, diatom biomass and carbon export in the northern South China Sea. Front. Earth Sc-Switz, 8, 537332, <https://doi.org/10.3389/feart.2020.537332>, 2020.

1175 Siegel, D. A., DeVries, T., Cetinić, I., Bisson, K. M.: Quantifying the ocean's biological pump and its carbon cycle impacts on global scales. Annu. Rev. Mar. Sci., 15(1), 329–356, <https://doi.org/10.1146/annurev-marine-040722-115226>, 2022.

1180 Stamieszkin, K., Poulton, N. J., Pershing, A. J.: Zooplankton grazing and egestion shifts particle size distribution in natural communities. Mar. Ecol. Prog. Ser., 575, 43–56, <https://doi.org/10.3354/meps12212>, 2017.

Steinberg, D. K., Stamieszkin, K., Maas, A. E., Durkin, C. A., Passow, U., Estapa, M. L., Omand, M. M., McDonnell, A. M. P., Karp-Boss, L., Galbraith, M., Siegel, D. A.: The oversized role of salps in carbon export in the subarctic northeast Pacific Ocean. Global Biogeochem. Cy., 37, e2022GB007523, <https://doi.org/10.1029/2022GB007523>, 2023.

1185 Stemmann, L., Eloire, D., Sciandra, A., Jackson, G. A., Guidi, L., Picheral, M., Gorsky, G.: Volume distribution for particles between 3.5 to 2000 μm in the upper 200 m region of the South Pacific Gyre. Biogeosciences, 5, 299–310, <https://doi.org/10.5194/bg-5-299-2008>, 2008.

Stramma, L., Bange, H. W., Czeschel, R., Lorenzo, A., Frank, M.: On the role of mesoscale eddies for the biological productivity and biogeochemistry in the eastern tropical Pacific Ocean off Peru. Biogeosciences, 10, 7293–7306, <https://doi.org/10.5194/bg-10-7293-2013>, 2013.

1190 [Trudnowska, E., Lacour, L., Ardyna, M., Rogge, A., Irissou, J. O., Waite, A. M., Babin, M., Stemmann, L.: Marine snow morphology illuminates the evolution of phytoplankton blooms and determines their subsequent vertical export. Nat. Commun., 12, 2816, https://doi.org/10.1038/s41467-021-22994-4, 2021.](https://doi.org/10.1038/s41467-021-22994-4)

1195 [Trudnowska, E., Błachowiak-Samołyk, K., Stemmann, L.: Structures of coexisting marine snow and zooplankton in coastal waters of Svalbard \(European Arctic\). Elem. Sci. Anth., 11\(1\), 00010, https://doi.org/10.1525/elementa.2023.00010, 2023.](https://doi.org/10.1525/elementa.2023.00010)

Turner, J. T.: Zooplankton fecal pellets, marine snow, phytodetritus and the ocean's biological pump. Prog. Oceanogr., 130, 205–248, <https://doi.org/10.1016/j.pcean.2014.08.005>, 2015.

1200 Turner, J. S., Pretty, J. L., McDonnell, A. M. P.: Marine particles in the Gulf of Alaska shelf system: Spatial patterns and size distributions from in situ optics. Cont. Shelf Res., 145, 13–20, <https://doi.org/10.1016/j.csr.2017.07.002>, 2017.

1205 [Wang, L., Huang, B. Q., Chiang, K. P., Liu, X., Chen, B. Z., Xie, Y. Y., Xu, Y. P., Hu, J. Y., Dai, M. H.: Physical-biological coupling in the western South China Sea: the response of phytoplankton community to a mesoscale cyclonic eddy. Plos One, 11\(4\), e0153735, https://doi.org/10.1371/journal.pone.0153735, 2016.](https://doi.org/10.1371/journal.pone.0153735)

Wang, X., Zhang, J., Zhao, X., Chen, Z., Ying, Y., Li, Z., Xu, D., Liu, Z., Zhou, M.: Vertical distribution and diel

带格式的：超链接，字体：（默认）Times New Roman，10 磅

域代码已更改

带格式的：字体：（默认）Times New Roman，10 磅

带格式的：字体：（默认）Times New Roman，10 磅

域代码已更改

带格式的：超链接，字体：（默认）Times New Roman，五号，字体颜色：自动设置，图案：清除

- migration of mesopelagic fishes on the northern slope of the South China Sea. *Deep-Sea Res. PT II*, 167, 128–141, <https://doi.org/10.1016/j.dsr2.2019.05.009>, 2019.
- 1210 Wang, X. Y., Li, H. L., Zhang, J. J., Chen, J. F., Xie, X. H., Xie, W., Yin, K. D., Zhang, D. S., Ruiz-Pino, D., Kao, S. J.: Seamounts generate efficient active transport loops to nourish the twilight ecosystem. *Sci. Adv.*, 10(26), eadk6833, [10.1126/sciadv.adk68](https://doi.org/10.1126/sciadv.adk68), 2024a.
- Wang, Z. Y., Fang, C., Yang, C. H., Zhang, G. Y., Sun, D.: Latitudinal gradient and influencing factors of deep-sea particle export along the Kyushu-Palau Ridge in the Philippine Sea. *Sci. Total Environ.*, 906, 167460, <https://doi.org/10.1016/j.scitotenv.2023.167460>, 2024b.
- 1215 Welschmeyer, N. A.: Fluorometric analysis of chlorophyll a in the presence of chlorophyll b and pheopigments. *Limnol. Oceanogr.*, 39(8), 1985–1992, <https://doi.org/10.4319/lo.1994.39.8.1985>, 1994.
- Wu, C. R., Chiang, T. L.: Mesoscale eddies in the northern South China Sea. *Deep-Sea Res. PT II*, 54(14-14), 1575–1588, <https://doi.org/10.1016/j.dsr2.2007.05.008>, 2007.
- 1220 Xu, W. L., Wang, G. F., Xing, X. G., Cornec, M., Hayward, A., Chen, B. Z., Chen, X. H.: Mesoscale eddies drive phytoplankton-mediated biogeochemistry in the South China Sea. *J. Geophys. Res.*, 130(6), e2024JG008664, <https://doi.org/10.1029/2024JG008664>, 2025.
- Xiu, P., Chai, F., Shi, L., Xue, H., Chao, Y.: A census of eddy activities in the South China Sea during 1993–2007. *J. Geophys. Res.*, 115, C03012, <https://doi.org/10.1029/2009JC005657>, 2010.
- Xiu, P., Chai, F.: Modeled biogeochemical responses to mesoscale eddies in the South China Sea. *J. Geophys. Res.*, 116, C10006, <https://doi.org/10.1029/2010JC006800>, 2011.
- 1225 Zhang, M., Wu, Y., Wang, F. Q., Xu, D. F., Liu, S. M., Zhou, M.: Hotspot of organic carbon export driven by mesoscale eddies in the slope region of the northern South China Sea. *Front. Mar. Sci.*, 7, 444, <https://doi.org/10.3389/fmars.2020.00444>, 2020.
- Zhang, W. J., Zhang, C., Zheng, S., Chen, Y. Y., Zhu, M. L., Sun, X. X.: Distribution of picophytoplankton in the northern slope of the South China Sea under environmental variation induced by a warm eddy. *Mar. Pollut. Bull.*, 194, 115429, <https://doi.org/10.1016/j.marpolbul.2023.115429>, 2023.
- Zhou, K. B., Dai, M. H., Maiti, K., Chen, W. F., Chen, J. H., Hong, Q. Q., Ma, Y. F., Xiu, P., Wang, L., Xie, Y. Y.: Impact of physical and biogeochemical forcing on particle export in the South China Sea. *Prog. Oceanogr.*, 187, 102403, <https://doi.org/10.1016/j.pocan.2020.102403>, 2020.
- 1235 Zhou, K. B., Benitez-Nelson, C. R., Huang, J., Xiu, P., Sun, Z. Y., Dai, M. H.: Cyclonic eddies modulate temporal and spatial decoupling of particulate carbon, nitrogen, and biogenic silica export in the North Pacific Subtropical Gyre. *Limnol. Oceanogr.*, 66(9), 3508–3522, <https://doi.org/10.1002/lno.11895>, 2021.

带格式的: 字体: (默认) Times New Roman

带格式的: 字体: (默认) Times New Roman, 10 磅

带格式的: 字体: (默认) Times New Roman, 10 磅

带格式的: 字体: (默认) Times New Roman, 10 磅